Optimized wavelet scales for damage detection in the laminated composite curved beams

Morteza Saadatmorad[1], Ali Ahmadi[2], Maryam Abedi[2], Ramazan-Ali Jafari-Talookolaei[3*], Sherzod Tadjibayev[4]

[1] Department of Civil, Chemical, Environmental and Materials Engineering, University of Bologna, Italy.
[2] Department of Engineering and Technology, University of Mazandaran, Babolsar, Iran.
[3] School of Mechanical Engineering, Babol Noshirvani University of Technology, Babol, Iran.
[4] Ecole Polytechnique, Route de Saclay, 91128 PALAISEAU Cedex, France.

*Corresponding Author: ramazanali@gmail.com, ra.jafari@nit.ac.ir

Abstract
Although the one-dimensional continuous wavelet transform (1D-CWT) often suffers from redundant scales when applied to structural damage detection, it remains a valuable tool due to its flexibility in selecting optimal wavelet functions for improved accuracy. This paper investigates the capability of 1D-CWT to accurately identify the most effective wavelet scales tailored for localizing damage in laminated composite curved beams, a complex structural element widely used in aerospace and civil engineering. The finite element method is utilized for obtaining detailed mode shapes of these curved beams, providing representative input signals for wavelet transform analysis. To address the challenge of redundant scales, we propose employing the standard deviation of wavelet coefficients as a sensitive and robust index to pinpoint scales that most effectively highlight damage-induced changes. This quantitative metric enables a systematic selection of optimal scales, improving detection performance. Comprehensive numerical simulations complemented by experimental validations confirm that this approach significantly enhances damage localization accuracy. Overall, the results demonstrate that incorporating the standard deviation criterion into the 1D-CWT framework enhances its practicality and reliability, thereby positioning it as a powerful tool for structural health monitoring of laminated composite curved beams.

Keywords: Damage detection; Laminated composite curved beam; One-dimensional wavelet transform; Optimal scales for wavelet functions; Standard deviation index.

1. Introduction

Composite structures have been widely used in numerous engineering disciplines, such as civil, mechanical, aerospace, and marine engineering, because of their superior characteristics like high stiffness and strength, fatigue resistance, and lightweight [1–5]. Laminated composite beams are one of the most commonly used laminated composite structures, and many studies have been conducted on their vibrational behavior [6, 7]. Laminated composite curved beams are susceptible to severe impacts and damage due to their lightweight nature and use in high-speed applications [8]. Therefore, effective damage detection in these structures is essential.

So far, numerous investigations have been done on damage detection of the laminated composite structures. Allen et al. [9] investigated damage detection in composite laminates using nonlinear guided wave mixing. They introduced a method for detecting delamination in composite laminates using the nonlinear response of Lamb waves. A transducer network scans the structure, transmitting and receiving dual guided waves. Interaction between these waves and any delamination created composite frequencies due to contact nonlinearity. A damage location imaging algorithm, based on cross-correlation analysis of envelope signals, was developed. Numerical verification using a validated finite element model confirmed the method's effectiveness in predicting damage location, even with small nonlinear component amplitudes. The method demonstrates potential as a technique requiring no initial data or reference measurements. Kahya et al. [10] presented a numerical procedure for detecting and quantifying damage in laminated composite beams with arbitrary lay-ups using limited vibration data and the Harmony Search (HS) optimization algorithm. Using frequencies and mode shapes as diagnostic parameters, the HS algorithm minimized two distinct objective functions to identify damage zones. Numerical simulations on composite beams with single and multiple damages demonstrated that the method successfully detected moderate-to-severe damage, even in the presence of noise. While its accuracy was decreased for multiple minor damages, the study suggested overcoming this limitation through hybridizing the metaheuristic algorithm, enhancing the objective function with additional vibration parameters (e.g., curvature or flexibility), or implementing multi-stage identification techniques. Katunin et al. [11] evaluated the effectiveness, operational complexity, and cost-efficiency of four non-destructive testing (NDT) techniques—PZT sensing, ultrasonic testing, thermography, and vibration-based inspection—for aerospace composite structures under realistic environmental conditions. Experimental testing was conducted on glass fiber-reinforced plastic (GFRP), hybrid aluminum-GFRP sandwich panels, and a carbon fiber-reinforced plastic vertical stabilizer section from a military aircraft that featured delamination and barely visible impact damage. The resulting comparative analysis successfully defined the specific capabilities, boundaries, and tailored applications of each NDT method for the early-stage detection and localization of structural flaws in aircraft components. Tran-Ngoc et al. [12] used a model of artificial neural networks improved with metaheuristic algorithms to enhance damage detection in composite beam and plates. Mallouli et al. [13] used the Finite Wave Element (FWE) technique in the time domain to detect impact damage on composite beams. Kahya et al. [14] presented an automated model updating approach for damage detection in laminated composite beams with multiple damages. Damages in this study were crack-shaped. Manoach et al. [15] proposed a vibration-based damage detection technique for composite beams subjected to temperature variations via the Poincaré map. Khatir et al. [16] developed a damage identification technique by combining the proper orthogonal decomposition method with the radial basis function to identify damage in a carbon fiber reinforced polymer composite beam. Loi et al. [17] conducted experimental research to detect impact damage on composite beams based on analysis of non-linearity with pulse excitation. Cao et al. [18] used progressive wavelet transformations for detecting damage on composite beams. Vo- Duy et al. [19] applied the damage locating vector method to detect damage on composite beams. The method was based on the flexibility change matrix. Lestari et al. [20] investigated the use of wave propagation analysis to identify damage in laminated composite beams. Torabi et al. [21] applied the moving support method for delamination detection in composite beams based on the first natural frequency. Fan et al. [22] used mode shapes to detect damag**e** on plate structures using the wavelet transform. After using mode shapes, some problems may arise. To fix this problem, Cao et al. [23] suggested an integrated wavelet transform technique by which the mode shape signals were modified and fed into the wavelet transform. Jiang et al. [24] presented a new crack detection method based on the slope of the mode shape fed into the complex continuous wavelet transform. Poudel et al. [25] used the difference function of the mode shape for identifying damage in beams. Other studies used the wavelet transform to detect damage in different structures [26-28].

In wavelet-based damage detection, most studies rely on trial-and-error simulations to determine the optimal wavelet function, which poses challenges for practical implementation. For instance, Vafaei et al. [29] proposed a Neuro-wavelet method for damage localization of cantilever structures. They expressed that there is no unit strategy for selecting the best wavelet functions, which is often performed based on trial-and-error efforts. Abdulkareem et al. [30] implied that an important challenge in the wavelet transform was to choose the most suitable analyzing wavelet function. They selected Paul's wavelet function for accurate damage detection after many trial-and-error simulations. In [31], a methodology for selecting optimal analyzing wavelet functions for structural damage identification in beam structures was proposed. The proposed method was based on the ratio of detail and approximation signals in the discrete wavelet transform. Ashory et al. [32] proposed a delamination detection strategy for laminated composite plates based on increasing the sensitivity of the wavelet transform to tiny damages. In their methodology, they introduced a novel index for selecting the optimal analyzing wavelet function based on the correlation of the strain energy of the mode shape and wavelet function. To obtain the correlation values, they converted the two-dimensional mode shape signal into a one-dimensional signal.

A key research gap is the reliance on inefficient trial-and-error methods for wavelet selection. Existing literature on structural damage detection using optimized wavelets focuses primarily on the wavelet function and its vanishing moments. This study expands upon those factors by also incorporating optimal scale selection via CWT. This paper uses one-dimensional continuous wavelet transform (1D-CWT) to extract the standard deviation of wavelet coefficients at different scales and minimizes them to discover the optimal scales and wavelet coefficients for structural damage detection. The rest of this paper is structured as follows. In Section 2, the methodology, covering formulations, the solution method, finite element modeling, and the governing equation of motion, damage application within the finite element model, one-dimensional continuous wavelet transforms, and standard deviation calculations are presented. Section 3 introduces the proposed approach. Results and discussion are presented in Section 4. Section 5 concludes the study.

2. Methodology

2.1 Basic Formulations

Imagine a laminated composite curved beam (LCCB), as shown in Fig. 1. The LCCB has a mean radius *R*, width *b*, angle θ_0, and thickness *h*. The considered typical intact LCCB is constructed with *N* orthotropic and linearly elastic laminated layers. A coordinate system (θ, β, and z) is fixed on the considered LCCB, as seen in Fig. 1. If a damaged LCCB has *N* layers, the thickness of each lamina is obtained from $h_i = \dfrac{h}{N}$.

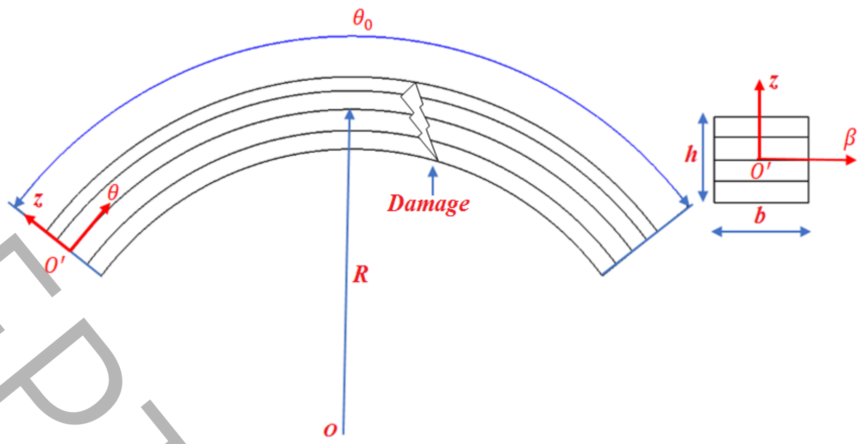

Fig. 1: A typical damaged LCCB with single damage

First, the basic formulations are derived for an intact LCCB. Then, the finite element model for damaged LCCB is developed by incorporating damage into this model.

Based on first-order shear deformation theory (FSDT), the following relations express displacement fields of the considered LCCB [33]:

$$u = u_0 + z\psi \qquad w = w_0 \tag{1}$$

where *u* and *w* denote displacement fields in the directions of the θ and *z*, respectively. Also, u_0 and w_0 show displacements at the mid-plane and ψ indicates bending rotation. Using Eq. (1) and by differentiation, the strain and curvature components are calculated as follows:

$$\varepsilon_\theta = \frac{1}{R}\frac{\partial u}{\partial \theta} + \frac{w}{R} \qquad \chi_\theta = \frac{1}{R}\frac{\partial \psi}{\partial \theta} \qquad \gamma_{\theta z} = \frac{1}{R}\frac{\partial w}{\partial \theta} - \frac{u}{R} + \psi \tag{2}$$

where χ_θ is curvature change, ε_θ denotes the normal strain, and $\gamma_{\theta z}$ shows the shear strain. The force and moment resultants are obtained as follows [34]:

$$\begin{Bmatrix} N_\theta \\ M_\theta \\ Q_\theta \end{Bmatrix} = \begin{bmatrix} A_{11} & B_{11} & 0 \\ B_{11} & D_{11} & 0 \\ 0 & 0 & A_{55} \end{bmatrix} \begin{Bmatrix} \varepsilon_\theta \\ \chi_\theta \\ \gamma_\theta \end{Bmatrix} \tag{3}$$

where N_θ, M_θ, and Q_θ represent the in-plane force, bending moment and shear force, respectively. Also, A_{11}, B_{11}, and D_{11} are the extensional stiffness, bending-extension coupling stiffness, and bending stiffness, respectively. Likewise, A_{55} indicates the shear stiffness. These stiffness coefficients are expressed as follows:

$$A_{11} = Rb\sum_{k=1}^{N} E_x^k \ln\left(\frac{R + z_{k+1}}{R + z_k}\right) \tag{4}$$

$$B_{11} = Rb\sum_{k=1}^{N} E_x^k \left[\left(z_{k+1} - z_k \right) - R\ln\left(\frac{R+z_{k+1}}{R+z_k} \right) \right] \tag{5}$$

$$A_{55} = k_s b\sum_{k=1}^{N} Q_{55}^k \left[\left(z_{k+1} - z_k \right) - \frac{4}{3h^2}\left\{ z_{k+1}^3 - z_k^3 \right\} \right] \tag{6}$$

$$D_{11} = Rb\sum_{k=1}^{N} E_x^k \left[\frac{\left(R+z_{k+1}\right)^2 - \left(R+z_k\right)^2}{2} - 2R\left(z_{k+1}-z_k\right) + R^2\ln\left(\frac{R+z_{k+1}}{R+z_k}\right) \right] \tag{7}$$

In a given layer k, z_{k+1} and z_k represent the distances along the z −axis to the top and bottom surfaces of the k^{th} layer from the mid-plane of the LCCB, respectively. Additionally, E_x^k is the equivalent modulus of elasticity as well as Q_{55}^k denotes the transformed shear stiffness of each lamina. Moreover, k_s shows the shear correction factor (considered to be 5/6 in this study). The following relation is governed on these quantities:

$$\frac{1}{E_x^k} = \frac{\cos^4\left(\vartheta_k\right)}{E_{11}^k} + \left(\frac{1}{G_{12}^k} - \frac{2\nu_{12}^k}{E_{11}^k} \right)\cos^2\left(\vartheta_k\right)\sin^2\left(\vartheta_k\right) + \frac{\sin^4\left(\vartheta_k\right)}{E_{22}^k} \tag{8}$$

$$Q_{55}^k = G_{13}^k \cos^2\left(\vartheta_k\right) + G_{23}^k \sin^2\left(\vartheta_k\right) \tag{9}$$

where E_{11}^k indicates the elasticity modulus of the LCCB in the direction parallel to fiber. E_{22}^k shows the elasticity modulus the LCCB in the direction normal to fiber and ν_{12} is the Poisson's ratio. Moreover, G_{ij}^k denotes the shear modulus in the *i*-direction on a plane whose normal is along the *j*-direction. Likewise, ϑ_k represents the fiber orientation of the k^{th} layer. In the present article, the penalty approach is employed to implement the boundary conditions. As depicted in Fig. 2, three springs are considered at both ends of the beam for the three displacement field variables (u, w, ψ) to apply the boundary condition. Based on the boundary conditions shown in Fig. 2, the potential energy of the boundary springs U_{AS} is formulated as follows:

$$U_{AS} = \frac{1}{2}\left[K_u^l u_0^2 + K_w^l w_0^2 + K_\psi^l \psi^2 \right]_{\theta=0} + \frac{1}{2}\left[K_u^r u_0^2 + K_w^r w_0^2 + K_\psi^r \psi^2 \right]_{\theta=\theta_0} \tag{10}$$

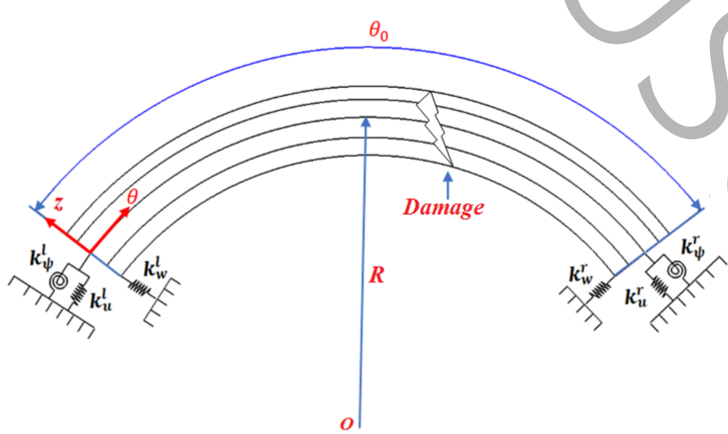

Fig. 2: General boundary conditions of the studied LCCB.

The potential energy of LCCB resulted from the strain energy is obtained as follows:

$$U_B = \frac{1}{2}\int_0^{\theta_0}\left(N_\theta \varepsilon_\theta + M_\theta \chi_\theta + Q_\theta \gamma_\theta\right) R d\theta \tag{11}$$

By substituting the Eqs. (2) and (3) into Eq. (11), the potential energy in terms of displacement components is rewritten as follows:

$$U_B = \frac{1}{2}\int_0^{\theta_0}\left[A_{11}\left(\frac{1}{R}\frac{\partial u_0}{\partial \theta}+\frac{w_0}{E}\right)^2 + 2B_{11}\frac{1}{R}\frac{\partial \psi}{\partial \theta}\left(\frac{1}{R}\frac{\partial u_0}{\partial \theta}+\frac{w_0}{R}\right) + D_{11}\left(\frac{1}{R}\frac{\partial \psi}{\partial \theta}\right)^2 + A_{55}\left(\frac{1}{R}\frac{\partial w_0}{\partial \theta}-\frac{u_0}{R}+\psi\right)^2\right] R d\theta \tag{12}$$

The kinetic energy of LCCB is expressed as follows:

$$T = \frac{1}{2}\int_0^{\theta_0}\left[\overline{I_0}\left(\frac{\partial u_0}{\partial t}\right)^2 + 2\overline{I_1}\frac{\partial u_0}{\partial t}\frac{\partial \psi}{\partial t} + \overline{I_2}\left(\frac{\partial \psi}{\partial t}\right)^2 + \overline{I_0}\left(\frac{\partial w_0}{\partial t}\right)^2\right] R d\theta \tag{13}$$

where the inertia terms are calculated as follows:

$$\begin{gathered}\overline{I_i} = I_i + \frac{I_{i+1}}{R} \quad (i = 0,1,2) \\ \left[I_0, I_1, I_2, I_3\right] = b\sum_{k=1}^{N}\int_{z_k}^{z_{k+1}} \rho_k \left[1, z, z^2, z^3\right] dz\end{gathered} \tag{14}$$

2.2. Solution Method

2.2.1. Finite Element Method

This section describes how to obtain the stiffness and mass matrices of a higher-order curved beam element. According to Fig. 3, each element's node contains three degrees of freedom (i.e., u_0, w_0, and ψ).

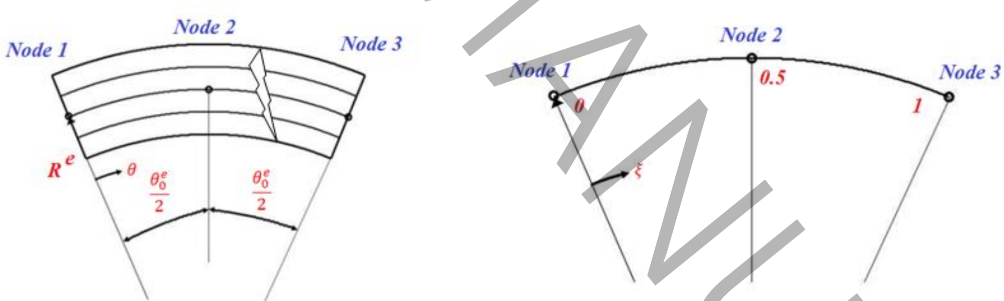

Fig. 3: Higher order curved beam's element used in the present study with the corresponding intrinsic coordinates

The displacement fields of the studied element can be interpolated as follows:

$$\begin{gathered}u_0 = \sum_{i=1}^{3} N_i(\xi) u_i \\ w_0 = \sum_{i=1}^{3} N_i(\xi) w_i \\ \psi = \sum_{i=1}^{3} N_i(\xi) \psi_i\end{gathered} \tag{15}$$

where ξ shows intrinsic coordinates. $N_i(\xi)$ denote the Lagrange interpolation functions obtained as follows:

$$\begin{aligned} N_1 &= 2\xi^2 - 3\xi + 1 \\ N_2 &= 4\left(\xi - \xi^2\right) \\ N_3 &= 2\xi^2 - \xi \end{aligned} \tag{16}$$

By rewriting potential and kinetic energies in terms of interpolation functions, the mass matrix $\mathbf{M^e}$ and the stiffness matrix $\mathbf{K^e}$ of the considered higher-order element of LCCB are obtained as:

$$\mathbf{M^e} = R\theta_0 \int_0^1 \begin{pmatrix} \overline{I_0}\,\mathbf{N_u}^T\mathbf{N_u} + \overline{I_1}\mathbf{N_u}^T\mathbf{N_\psi} + \overline{I_1}\mathbf{N_\psi}^T\mathbf{N_u} \\ +\overline{I_2}\mathbf{N_\psi}^T\mathbf{N_\psi} + \overline{I_0}\mathbf{N_w}^T\mathbf{N_w} \end{pmatrix} d\xi \tag{17}$$

$$\mathbf{K^e} = \int_0^1 \begin{pmatrix} \frac{A_{11}}{R\theta_0}\mathbf{N_{u,\theta}}^T\mathbf{N_{u,\theta}} + \frac{A_{11}\theta_0}{R}\mathbf{N_w}^T\mathbf{N_w} + \frac{A_{11}}{R}\mathbf{N_{u,\theta}}^T\mathbf{N_w} + \frac{A_{11}}{R}\mathbf{N_w}^T\mathbf{N_{u,\theta}} \\ +\frac{B_{11}}{R\theta_0}\mathbf{N_{\psi,\theta}}^T\mathbf{N_{u,\theta}} + \frac{B_{11}}{R\theta_0}\mathbf{N_{u,\theta}}^T\mathbf{N_{\psi,\theta}} + \frac{B_{11}}{R}\mathbf{N_{\psi,\theta}}^T\mathbf{N_w} + \frac{B_{11}}{R}\mathbf{N_w}^T\mathbf{N_{\psi,\theta}} \\ +\frac{D_{11}}{R\theta_0}\mathbf{N_{\psi,\theta}}^T\mathbf{N_{\psi,\theta}} + \frac{A_{55}}{R\theta_0}\mathbf{N_w}^T\mathbf{N_w} + \frac{A_{55}\theta_0}{R}\mathbf{N_{u,\theta}}^T\mathbf{N_{u,\theta}} + A_{55}R\theta_0\mathbf{N_{\psi,\theta}}^T\mathbf{N_{\psi,\theta}} \\ -\frac{A_{55}}{R}\mathbf{N_{w,\theta}}^T\mathbf{N_{u,\theta}} - \frac{A_{55}}{R}\mathbf{N_u}^T\mathbf{N_{w,\theta}} - A_{55}R\,\mathbf{N_{w,\theta}}^T\mathbf{N_\psi} - A_{55}R\,\mathbf{N_\psi}^T\mathbf{N_{w,\theta}} \\ -A_{55}\theta_0\mathbf{N_u}^T\mathbf{N_\psi} - A_{55}\theta_0\mathbf{N_\psi}^T\mathbf{N_u} \end{pmatrix} d\xi \tag{18}$$

where:

$$\begin{aligned} \mathbf{N_u} &= \begin{bmatrix} N_1 & 0 & 0 & N_2 & 0 & 0 & N_3 & 0 & 0 \end{bmatrix} \\ \mathbf{N_w} &= \begin{bmatrix} 0 & N_1 & 0 & 0 & N_2 & 0 & 0 & N_3 & 0 \end{bmatrix} \\ \mathbf{N_\psi} &= \begin{bmatrix} 0 & 0 & N_1 & 0 & 0 & N_2 & 0 & 0 & N_3 \end{bmatrix} \end{aligned} \tag{19}$$

2.2.2. Governing Equations of Motion

The total stiffness matrix $\mathbf{K}$ and total mass matrix $\mathbf{M}$ can be obtained from assembling the element's stiffness matrix and element's mass matrix, respectively. The elasticity coefficients are entered into their corresponding diagonal arrays in the total stiffness matrix to apply the effects of the boundary conditions. Next, the equation of motion of the whole system concerning the free vibration can be expressed as follows:

$$\mathbf{M}\,\ddot{\mathbf{\Delta}} + \mathbf{K}\,\mathbf{\Delta} = \mathbf{0} \tag{20}$$

where $\mathbf{\Delta}$ contains the degrees of freedom related to total nodes of the formed finite element model. In addition, by considering $\mathbf{\Delta} = \mathbf{\Delta_0}e^{i\omega t}$ and $\lambda = \omega^2$, Eq. (20) is written as follows:

$$(\mathbf{K} - \lambda\mathbf{M})\mathbf{\Delta_0} = 0 \tag{21}$$

where $\mathbf{\Delta_0}$ involves the mode shapes of the LCCB and ω is the corresponding natural frequencies. The solution of Eq. (21) can be obtained through solving det($\mathbf{K} - \lambda\mathbf{M}$)=0. This process is programmed in MATLAB software.

2.2.3. Applying Damages on the Finite Element Model

In order to introduce damage into the finite element model, prior to the assembly of the global stiffness matrix, a damage index α $(0 < \alpha < 1)$ is applied by multiplying the element stiffness matrix $\mathbf{K^e}$ [9]:

$$\mathbf{K^e}_\mathbf{d} = \alpha\mathbf{K^e} \Rightarrow D = (1-\alpha)\times 100 \tag{22}$$

where $\mathbf{K}^{\mathbf{e}}{}_{\mathbf{d}}$ is the stiffness matrix of a damaged element in the LCCB.

In the present study, damage is modeled as a localized reduction in the elastic modulus. This modeling approach is widely used in vibration-based structural health monitoring, since different physical damage mechanisms—such as cracks, delamination, and local section loss—ultimately manifest as a reduction in local stiffness and introduce changes in the structural dynamic response. Therefore, the adopted modeling strategy provides a generalized representation of damage effects at the structural level. Nevertheless, different damage mechanisms may generate distinct local dynamic signatures and severity distributions. Consequently, extending the proposed framework to explicitly model crack- and delamination-type damage constitutes an important direction for future research.

2.3 One-dimensional Continuous Wavelet Transform

It is proved that the wavelet transforms are simple and powerful tools for identifying damages in various structural elements. Based on the structural signal obtained from the different structures, three different types of wavelet transform are used to detect damages in the signals: one-dimensional wavelet transforms, two-dimensional wavelet transforms, and three-dimensional wavelet transform. In the case of beam structures modeled with one-dimensional finite elements, the obtained signals can be treated as one-dimensional. There are two types of one-dimensional wavelet transforms: one-dimensional discrete wavelet transforms (1D-DWT), and one-dimensional continuous wavelet transforms (1D-CWT). In this paper, 1D-CWT is used to detect damages in laminated composite curved beams.

Consider a one-dimensional signal $f(x)$ containing a subtle change or damage. In order to detect this subtle change, we need to transform its values into other space, where a wavelet function $\Psi(x)$ performs this. The following relation shows the expression of wavelets in real space in Hilbert space ($\Psi(x) \in L^2(\mathbb{R})$):

$$\Psi(x)_{u,s} = \frac{1}{\sqrt{s}}\psi\left(\frac{x-u}{s}\right) \tag{23}$$

where x is the spatial variable of the original signal $f(x)$, s and u denote scaling and shifting parameters, and s is a real number. It is noted that the average value of a wavelet function is zero. By applying the inner product of the wavelet functions $\Psi(x)_{u,s}$ with the original signal $f(x)$, wavelet coefficients $C(u,s)$ are obtained as follows [31]:

$$C(u,s) = \left\langle f, \Psi(x)_{u,s} \right\rangle = \frac{1}{\sqrt{s}}\int_{-\infty}^{+\infty} f(x)\Psi\left(\frac{x-u}{s}\right)dx \tag{24}$$

The main task of wavelet coefficients is to magnify subtle variations in the domain u with various different scales s.

Wavelet coefficients can be expressed in a convolution product form as follows [33, 35]:

$$C(u,s) = \left\langle f, \Psi(x)_{u,s} \right\rangle = \frac{1}{\sqrt{s}} f * \Psi\left(\frac{-u}{s}\right) \tag{25}$$

The accuracy of results from wavelet coefficients heavily depends on vanishing moments. When a wavelet has n vanishing moments, then the bellow expression has to be satisfied:

$$\int_{-\infty}^{+\infty} x^k \Psi(x)\,dx = 0, \quad k = 0,1,2,\ldots,n-1 \tag{26}$$

According to [۳۶], the Symlet wavelet function is an optimal function for vibration-based damage localization in composite structures. Thus, the Symlet wavelet function is used for the numerical and experimental evaluations.

3. Proposed Methodology

This section deals with research methodology. In our proposed methodology, mode shape signals obtained from finite element model or experimental modal analysis are used as the input signals. Then, the standard deviation filter is applied to each scale of wavelet coefficients to form a vector of standard deviation. Finally, the standard deviation vector is optimized to discover the minimum standard deviation that leads to the optimum wavelet coefficients for structural damage detection. A parametric study is performed using analysis of the obtained results for different wavelet functions with different vanishing moments for the considered scales. We describe this procedure mathematically in the following.

Consider 1D-CWT wavelet coefficients matrix $D_{m\times n}$ as follows:

$$\mathbf{D_{m\times n}} = \begin{bmatrix} d_{1,1} & d_{1,2} & d_{1,3} & & d_{1,n-2} & d_{1,n-1} & d_{1,n} \\ d_{2,1} & d_{2,2} & d_{2,3} & \cdots & d_{2,n-2} & d_{2,n-1} & d_{2,n} \\ d_{3,1} & d_{3,2} & d_{3,3} & & d_{3,n-2} & d_{3,n-1} & d_{3,n} \\ & \vdots & & \ddots & & \vdots & \\ d_{m-2,1} & d_{m-2,2} & d_{m-2,3} & & d_{m-2,n-2} & d_{m-2,n-1} & d_{m-2,n} \\ d_{m-1,1} & d_{m-1,2} & d_{m-1,3} & \cdots & d_{m-1,n-2} & d_{m-1,n-1} & d_{m-1,n} \\ d_{m,1} & d_{m,2} & d_{m,3} & & d_{m,n-2} & d_{m,n-1} & d_{m,n} \end{bmatrix} \tag{27}$$

We compute the standard deviation of each scale. Because the 1D-CWT wavelet coefficients are two-dimensional, we have to compute the standard deviation of the matrix. For this, we compute the standard deviation of each row of the 1D-CWT wavelet coefficients at first as follows:

$$
\mathbf{C}=\begin{Bmatrix} C_1 \\ C_2 \\ C_3 \\ \vdots \\ C_{m-2} \\ C_{m-1} \\ C_m \end{Bmatrix}=\begin{Bmatrix} \sqrt{\frac{1}{n-1}\sum_{i=1}^{n}\left|d_{1,i}-\frac{1}{n-1}\sum_{i=1}^{n}d_{1,i}\right|^2} \\ \sqrt{\frac{1}{n-1}\sum_{i=1}^{n}\left|d_{2,i}-\frac{1}{n-1}\sum_{i=1}^{n}d_{2,i}\right|^2} \\ \sqrt{\frac{1}{n-1}\sum_{i=1}^{n}\left|d_{3,i}-\frac{1}{n-1}\sum_{i=1}^{n}d_{3,i}\right|^2} \\ \vdots \\ \sqrt{\frac{1}{n-1}\sum_{i=1}^{n}\left|d_{m-2,i}-\frac{1}{n-1}\sum_{i=1}^{n}d_{m-2,i}\right|^2} \\ \sqrt{\frac{1}{n-1}\sum_{i=1}^{n}\left|d_{m-1,i}-\frac{1}{n-1}\sum_{i=1}^{n}d_{m-1,i}\right|^2} \\ \sqrt{\frac{1}{n-1}\sum_{i=1}^{n}\left|d_{m,i}-\frac{1}{n-1}\sum_{i=1}^{n}d_{m,i}\right|^2} \end{Bmatrix} \quad \text{28)}
$$

Finally, the standard deviation of the detail matrix is computed as follows:

$$
\mathbf{C}^{*}=\min\begin{Bmatrix} C_1 \\ C_2 \\ C_3 \\ \vdots \\ C_{m-2} \\ C_{m-1} \\ C_m \end{Bmatrix} \quad (29)
$$

We select the detail signal with an optimal wavelet function that provides the minimum standard deviation for local subtle damage detection objectives. A theoretical justification of the standard deviation criterion is that, in general, a smaller standard deviation in the wavelet coefficient vector A compared to vector B indicates that A's values are more stable and concentrated around their mean, while B exhibits greater fluctuations and dispersion. In signal processing, this often implies that A is smoother, has reduced high-frequency noise, or is subject to damping. Mathematically, A's smaller standard deviation signifies that the sum of squared distances from its points to its mean is less than that of B. Graphically, aside from the damage point, other aspects exhibit changes within shorter intervals and smaller ranges. Consequently, the range difference at the damage location is amplified compared to the function's overall change range. Fig. 4 shows the flowchart of the proposed damage detection technique.

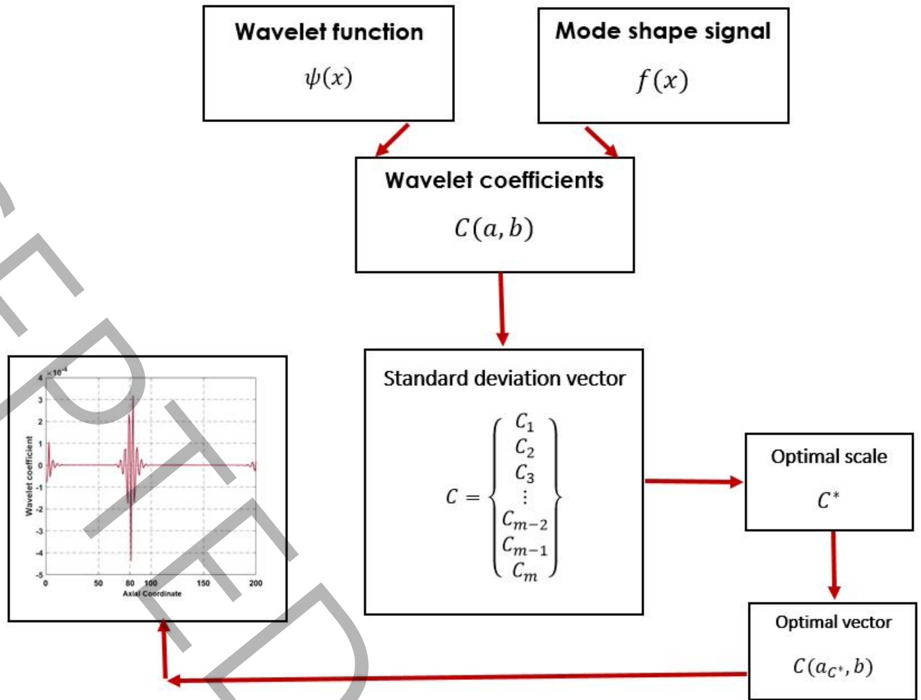

Fig. 4: Flowchart of the proposed damage detection technique

4. Results and Discussions

In this section, the results of the present study are presented. First, the results of the developed finite element model are validated against available literature. Then, the effect of damage on natural frequencies and mode shapes in the LCCB is investigated. Then, the numerical and experimental performances of the proposed method are evaluated.

4.1. Performance of the Finite Element Model

To verify the accuracy of the finite element method program developed in the present study, the results obtained for an LCCB with the properties listed in Table 1 are compared with the corresponding results reported in Refs. [37] and [38].

Table 1: Geometrical and material properties of the considered LCCB

$R=1\ m$	$\theta_0 = \frac{2\pi}{3} rad$	$G_{13} = 5.5 GPa$	$E_{22} = 10 GPa$
$\nu_{12} = 0.27$	$\rho = 1700 \frac{kg}{m^3}$	$layup\ [0°/90°]$	

Note that boundary conditions considered in this section are clamped-clamped (CC) and simple-simple (SS). In Table 2, the dimensionless fundamental frequency ($\Omega = \omega R^2 \theta_0^2 \sqrt{12\rho/(E_{11}h^2)}$) of the curved beam is presented for two types of boundary conditions and for three ratios of h/R. As observed, the present results show a very good agreement with the results reported in other studies.

Table 2: Comparison of dimensionless fundamental frequencies (Ω) ($\frac{E_{11}}{E_{22}}=15$)

Boundary Conditions	SS			CC	
h/R	Present	[37]	[38]	Present	[37]
0.05	14.905	14.880	14.891	24.680	24.681
0.1	14.977	14.964	14.976	23.617	23.490
0.15	14.834	14.768	14.779	21.920	21.655

4.2. The effect of damage on mode shapes

This section investigates the effect of damage on mode shapes. Figs. 5a-d provide a comparison between intact and damaged mode shapes corresponding to the first three natural frequencies in an arbitrary LCCB.

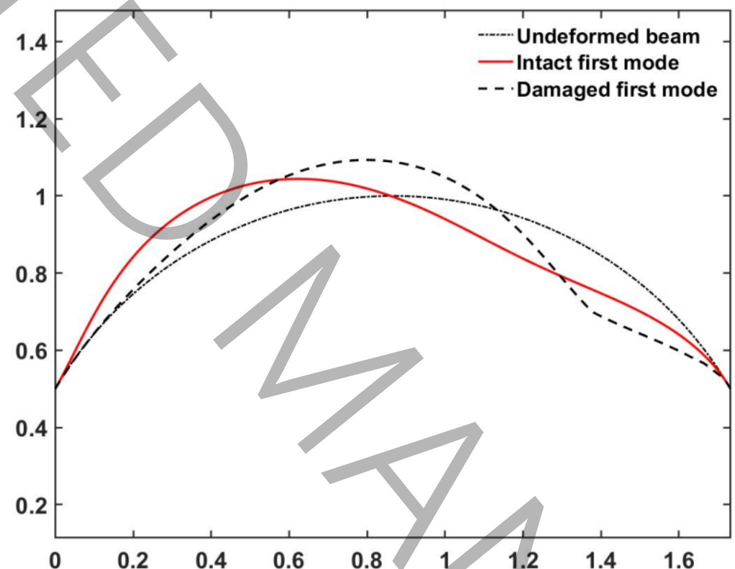

a) Red line: first mode shape of the intact LCCB; dashed black line: first mode shape of the damaged LCCB.

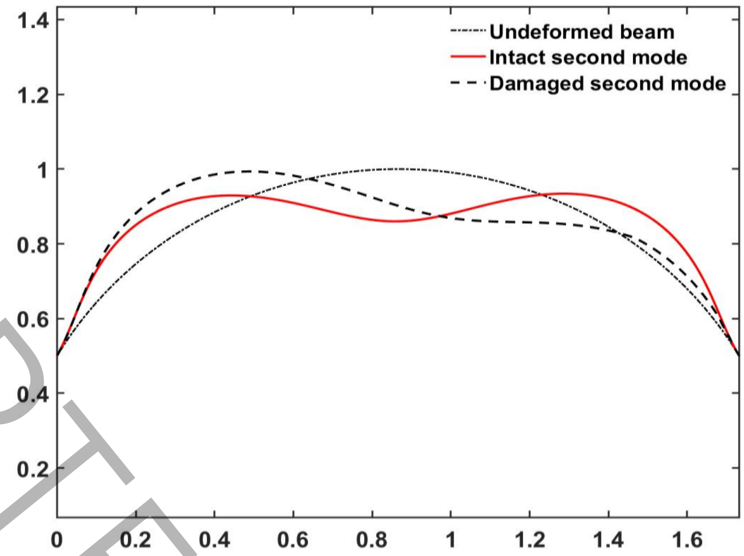

b) Red line: second mode shape of the intact LCCB, dashed black line: second mode shape of the damaged LCCB.

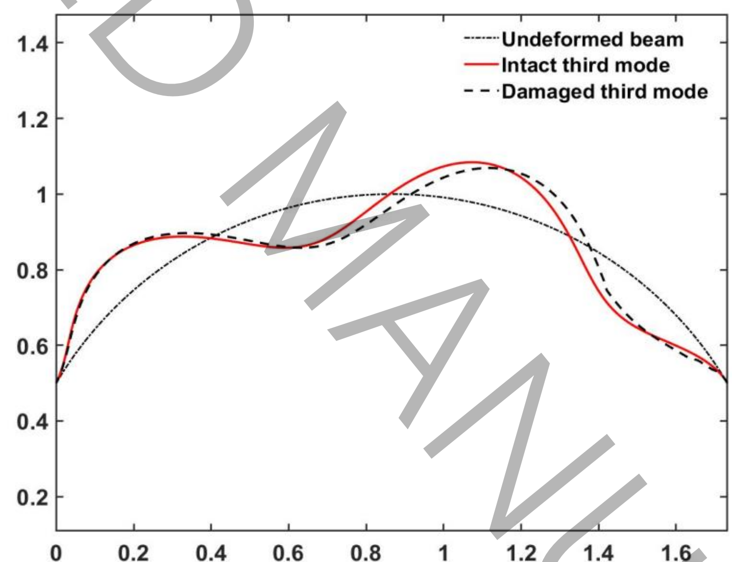

c) Red line: third mode shape of the intact LCCB; dashed black line: third mode shape of the damaged LCCB.

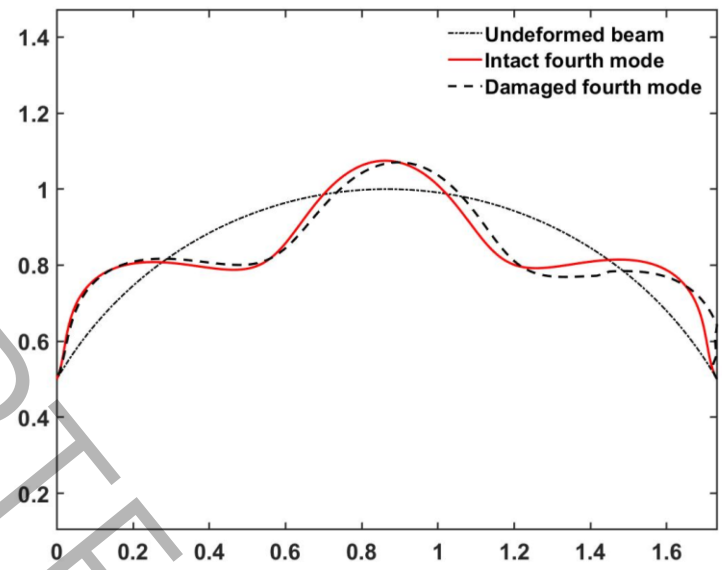

d) Red line: fourth mode shape of the intact LCCB; dashed black line: fourth mode shape of the damaged LCCB.

Fig. 4: Comparison between the first four intact and damaged mode shapes in an arbitrary LCCB.

As shown in Fig. 4, damage causes a shift in damaged mode shapes compared to intact mode shapes in all modes. It is consistent with the results presented in the literature on damage detection. Therefore, damaged mode shapes are a proper index for understanding the existence of damage, but they are not a suitable damage index for finding the exact location of damages. Therefore, this paper proposes a novel and efficient damage detection technique for damage detection on laminated composite curved beams.

4.3. Performance of the Proposed Method

To demonstrate the accuracy and efficiency of the damage localization approach proposed in the current paper, numerical and experimental damage detection scenarios in the form of single damages and multiple damage scenarios are presented.

4.3.1. Numerical Evaluation

Table 3 denotes the numerical damage scenarios considered in this study. The damages' locations are listed in node coordinates and element coordinates. Note that the results reported in this paper are based on node coordinates because mode shapes' signals consist of nodal displacements.

Table 3: Damage scenarios for single damages

Scenario No.	Location of Single Damages	Damage Level	Number of Nodes (n)
	Damaged Nodes Coordinates		
1	79, 80, 81	10%	201
2	79, 80, 81	85%	201
3	79, 80, 81	35%	201
4	119, 120, 121	90%	201

5	119, 120, 121	70%	201
6	119, 120, 121	50%	201

Damage scenarios for single damages are listed in Table 3. As mentioned, and shown in Fig. 4, the higher-order curved beam's element is used in the present study. Each element has three nodes. Thus, if L is the number of elements and n is the number of nodes, then for an LCCB with L elements, we have n=2L+1 nodes. Therefore, in Table 3, damages' locations are listed in nodes coordinates and element coordinates. Note that the results reported in this paper are based on node coordinates because mode shapes' signals consist of nodal displacements.

Fig. 5 shows the results obtained from the1D-CWT. These images are presented in the form of 3D and front views. The wavelet functions used in these transforms are selected randomly. As shown in Fig. 5, the damages are not detected in the six scenarios using the 1D-CWT due to the scales' redundancy. In other words, damage can be localized at a specific scale by a given wavelet function. However, according to our methodology, it is possible to detect damage location by having these results. We suggest filtering these coefficients using the standard deviation index to discover the optimal wavelet function and its scale.

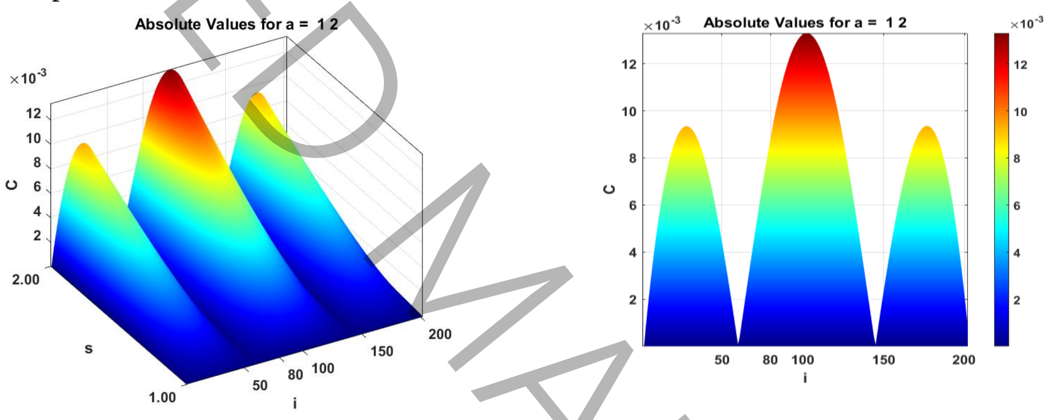

3D view front view

Scenario 1

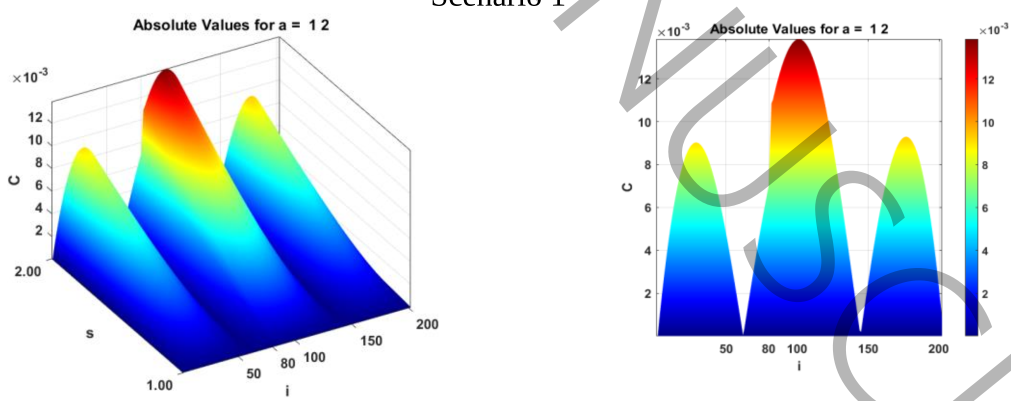

3D view front view

Scenario 2

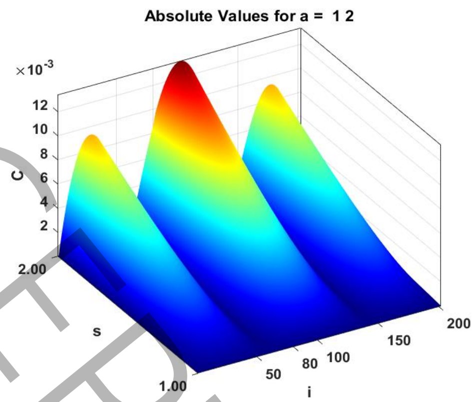

3D view

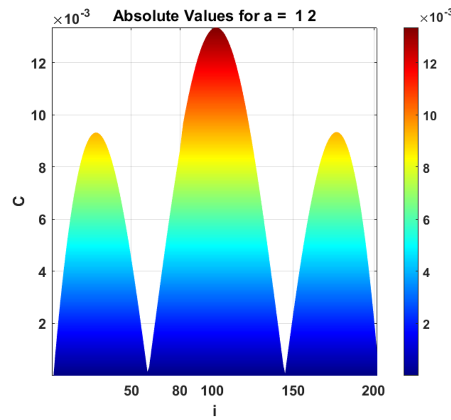

front view

Scenario 3

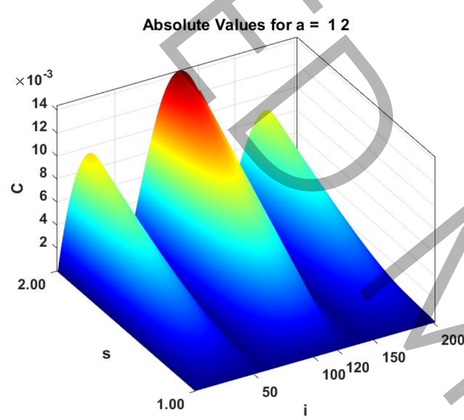

3D view

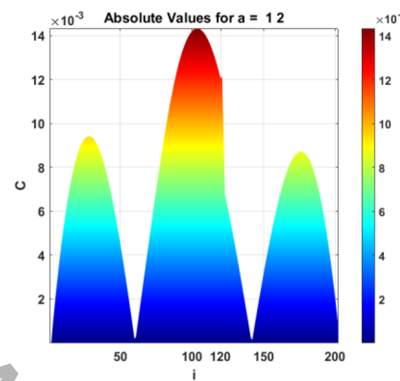

front view

Scenario 4

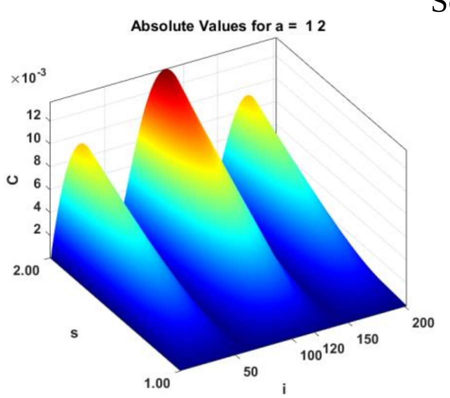

3D view

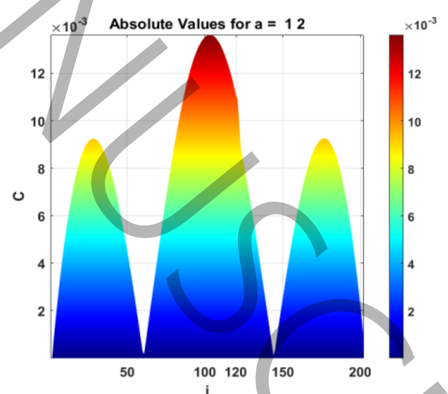

front view

Scenario 5

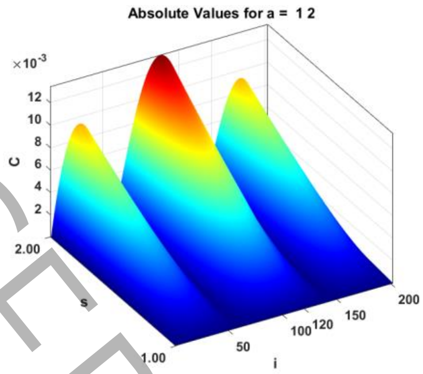

3D view

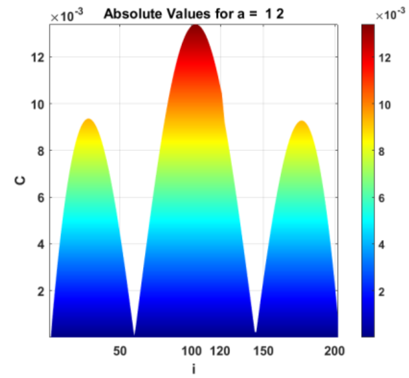

front view

Scenario 6

Fig. 5: Results obtained from the conventional 1D-CWT for six single damages scenarios.

Because the damage creates a local high-frequency component in the mode shape signal, only the lower scales contain information about the damage. Therefore, in this study, we examine the standard deviation of the wavelet coefficients on scales 1 to 5. Table 4 shows the calculated standard deviations for the first scenario using different wavelet functions. The minimum value obtained for each wavelet function between these five scales is specified by the symbol (*). Note that wavelet analysis uses various wavelet functions tailored for specific applications. The Haar wavelet, being the simplest, excels at detecting abrupt signal changes due to its discontinuous, piecewise constant nature; however, it is less effective for smooth approximations. Symlet and Daubechies wavelets offer near-symmetry, balancing space and frequency localization for signal compression and noise reduction. Coiflet wavelets, with vanishing moments in both mother and scaling functions, are more symmetric and better approximate smooth data. Bi-orthogonal wavelets utilize separate decomposition and reconstruction wavelets, allowing for perfect reconstruction and linear phase symmetry.

Table 4: Standard deviations of the wavelet coefficients corresponding to the first five scales for scenario 1

Scale 1	Scale 2	Scale 3	Scale 4	Scale 5
		Haar		
1.17e-18*	0.007936	0.012962	0.022434	0.030066
		Sym2		
0.001874	0.000307*	0.000999	0.001719	0.002988
		Sym3		
6.93e-05	2.95E-05*	0.000214	0.00024	0.000568
		Sym4		
0.000993	2.24E-05*	8.84E-05	0.000141	0.000283
		Sym5		
0.00194	1.84E-05*	0.000253	0.000125	0.000262
		Coif1		
0.000204*	0.000294	0.000828	0.001648	0.002875
		Coif2		
9.45e-05	2.11e-05*	6.95e-05	0.000138	0.000262
		Coif3		

6.85e-05	1.76e-05 *	5.44e-05	0.000107	0.000195
Coif4				
6.60e-05	1.64e-05 *	4.90e-05	9.78e-05	0.000177
Bior1.3				
1.02e-06*	0.007936	0.013922	0.022445	0.030982
Bior1.5				
1.96e-06*	0.007936	0.014288	0.022445	0.031219
Bior2.4				
0.000166*	0.00018	0.000573	0.001012	0.001738
Bior3.9				
0.007061	3.15e-05*	0.000647	0.000138	0.000408

In order to better imagination, we draw the data related to the Table 4 in Fig. 6. These diagrams plot the standard deviation versus the scales. Results for each wavelet function family are plotted separately. Several explanations can be stated through these results. First, in scales more than 3, as the scales increases, the standard deviation increases. Hence, the higher scales more than 3 are not appropriate for structural damage detection. Fig. 6 demonstrates that scales 1 and 2 are candidates for being the optimal wavelet scales for efficient damage detection since the standard deviation of wavelet coefficients obtained from the 1D-CWT has its minimum value. In these results, Sym, Coif, and Bior are the abbreviated names for Haar, Symlet, Coiflet, and Bi-orthogonal wavelet functions. Also, for example, Sym2 means a Symlet wavelet function with maximum vanishing moments equal to 2. An interesting finding is that, with the exception of the first scale, as the vanishing moments of a wavelet at a specific family increase, the standard deviation value at all scales tends to be lower, and the lower standard deviation leads to a more optimal wavelet function for structural damage detection. Therefore, we suggest using the wavelet function with higher vanishing moments for structural damage function purposes. We also can observe the range of the standard deviations in terms of scales for different wavelet families to select the best wavelet family. Thus, the optimal wavelet family can be selected via the standard deviation.

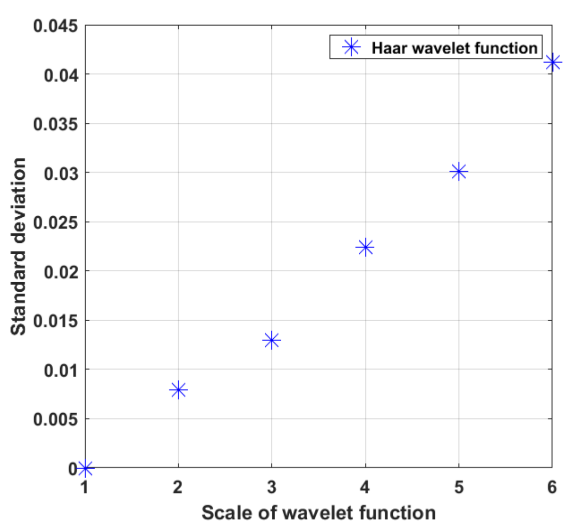

A

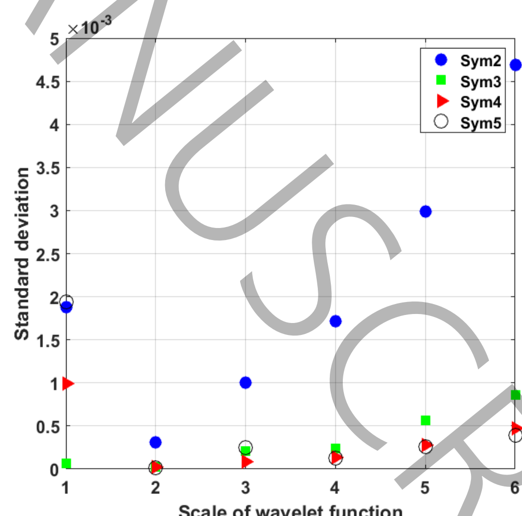

b

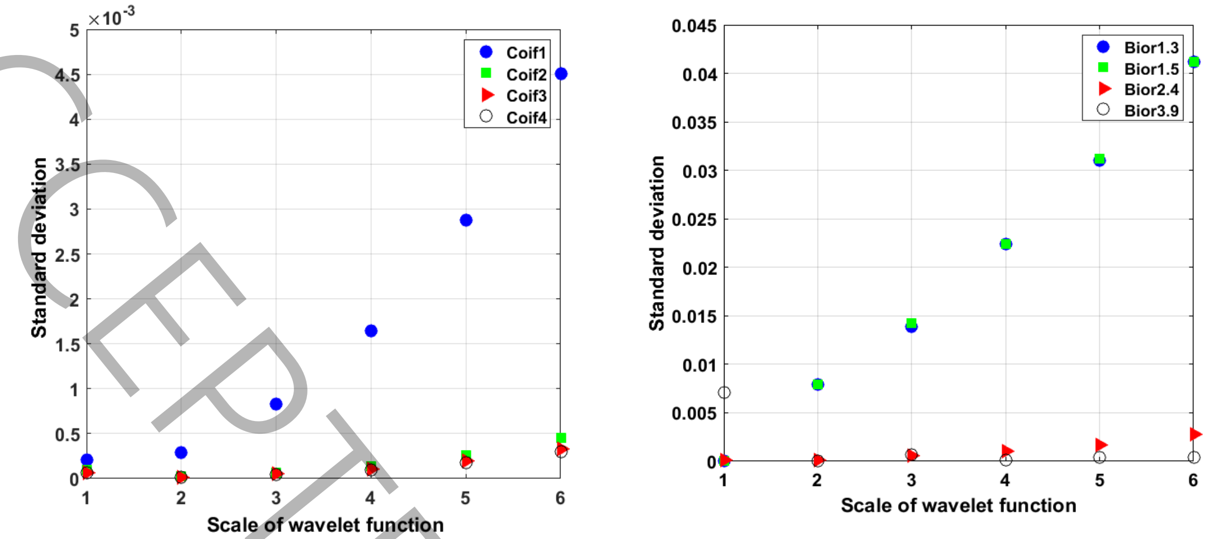

C d

Fig. 6: Standard deviation obtained from different families of wavelet functions at different scales for scenario 1

We use two families of wavelet functions at different scales to compare their performance and evaluate the effect of standard deviation and different scales on the precision of damage detection on the laminated composite curved beam. Fig. 7 shows the results of damage detection for scenario 1 using the family of wavelet functions Sym at various scales. Fig. 7 proves that scale 2 is optimal for the wavelet family Sym 2. According to Table 4, scale 2 has the minimum value of standard deviation related to wavelet coefficients for the wavelet family Sym 2. Another interesting result is that the wavelet function Sym 3 with scale 3 is more optimal than the wavelet function Sym 2 with scale 2; because this wavelet function at scale 3 has a smaller value of standard deviation compared to the wavelet function Sym 2 with scale 2 (according to Table 4). Thus, findings demonstrate that as the vanishing moments of a family of wavelet functions increase, the standard deviation of the wavelet coefficients produced by them decreases, and as a result, the accuracy of damage detection increases. Note that we cannot conclude that a wavelet function from a family is more optimal than another wavelet function from another family merely by comparing the standard deviation because the waveform of each family is different.

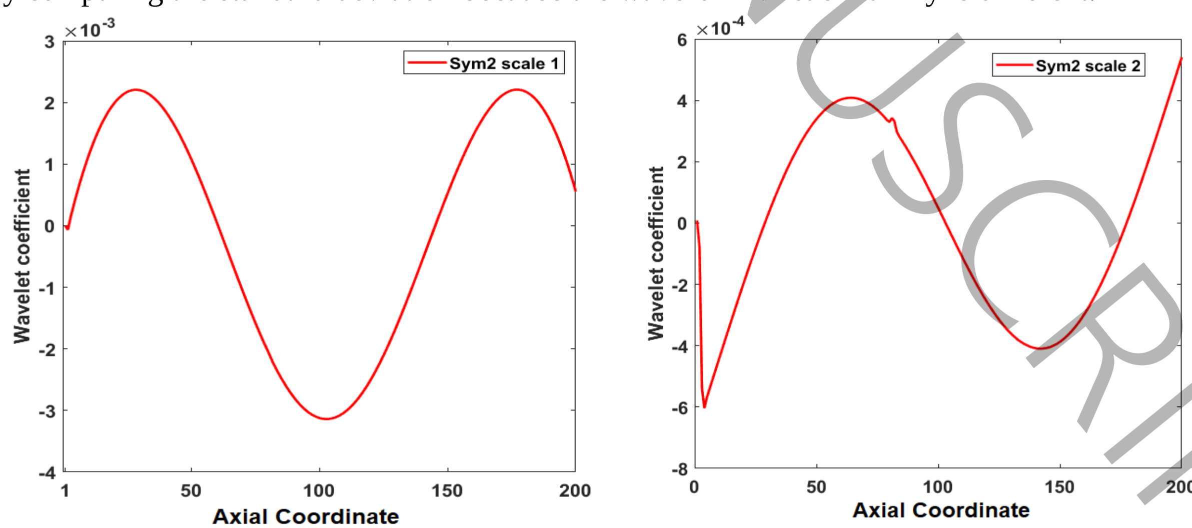

a

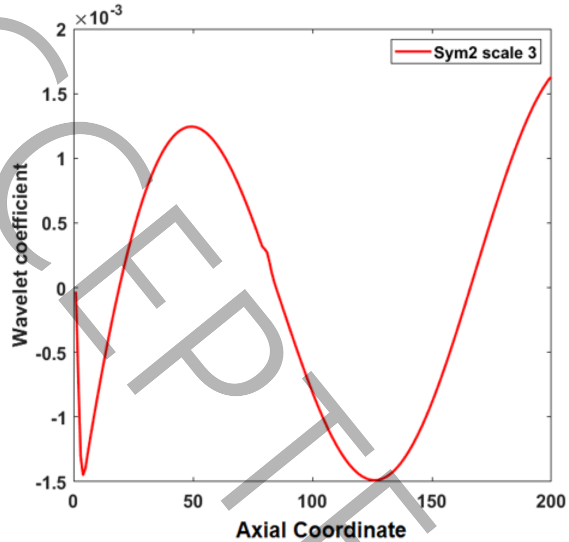

b

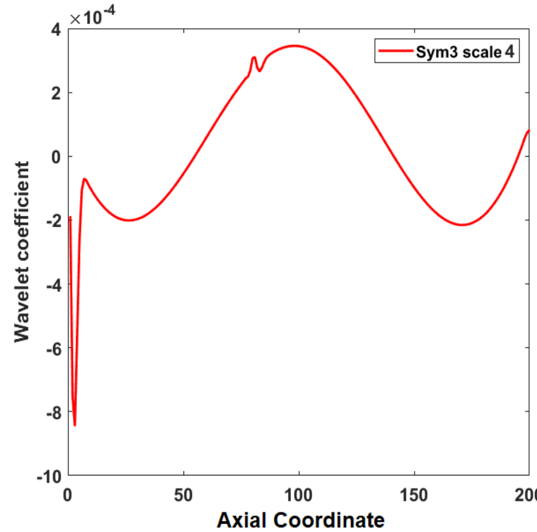

c

d

Fig. 7: Results of damage detection using the family of wavelet functions Symlet at different scales. a) Symlet wavelet function with vanishing moments 2 and scale 1, b) Symlet wavelet function with vanishing moments 2 and scale 2, c) Symlet wavelet function with vanishing moments 2 and scale 3, and d) Symlet wavelet function with vanishing moments 3 and scale 3

For another example, we consider the results of Table 4 for the family of wavelet function Coiflet, as seen in Fig. 8. We compare wavelet functions Coif with vanishing moments 1 and 4 with the scales 1 and 2 as well as 2 and 4. Graphical results presented in Fig. 8 indicate that among these four plots, the best wavelet function is Coif 4 with scale 2. This result is in good agreement with Table 4 and Fig. 6c. The results presented in this figure are consistent with the conclusions mentioned for the previous figure. In other words, as the vanishing moments of a family of wavelet functions increase, the standard deviation of the wavelet coefficients produced by them decreases, hence, the precision of damage detection increases.

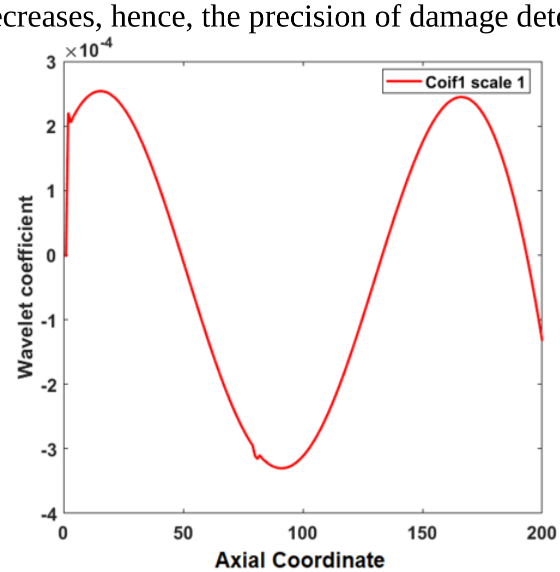

A

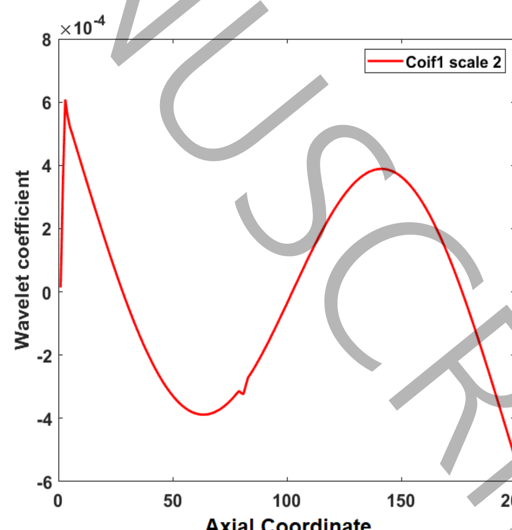

b

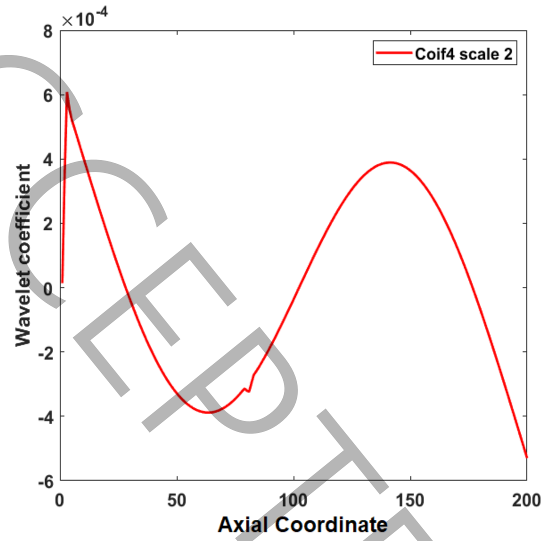

C

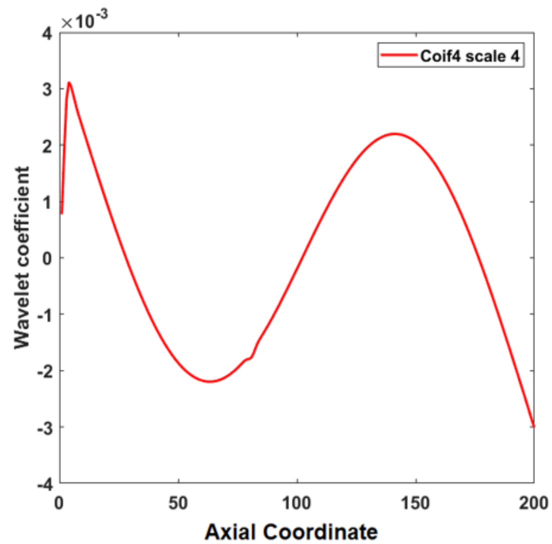

d

Fig. 8: Results of damage detection using the family of wavelet functions Coiflet at different scales. a) Coiflet wavelet function with vanishing moments 1 and scale 1, b) Coiflet wavelet function with vanishing moments 1 and scale 2, c) Coiflet wavelet function with vanishing moments 4 and scale 2, and d) Coiflet wavelet function with vanishing moments 4 and scale 4.

Table 5 lists the obtained standard deviations for the second scenario for different wavelet functions. The minimum value obtained for each wavelet function between these five scales is differentiated by the symbol (*).

Table 5: Standard deviations obtained from the wavelet coefficients related to the first five scales for scenario 2

Scale 1	Scale 2	Scale 3	Scale 4	Scale 5
		Gaus1		
0.017964*	0.05074	0.092948	0.142272	0.198149
		Gaus2		
0.000488125*	0.002673057	0.007200622	0.014532801	0.024933098
		Gaus3		
9.85e-05*	0.000384389	0.001030326	0.001946795	0.003925571
		Gaus4		
2.84e-05*	0.000209554	0.000514086	0.000977868	0.00165393
		Mexh		
0.001139933*	0.006215127	0.016736564	0.033584409	0.057532796
		Meyr		
0.00031042*	0.00043653	0.000948612	0.001010056	0.001476836
		Dmey		
0.000770952	5.13**e**-05*	0.000144528	0.000273863	0.000442893
		Morl		
0.000137	3.28**e**-05*	0.00011	0.000202	0.000344
		Db1		
1.18e-18*	0.008009915	0.013082571	0.022642119	0.030343834
		Db2		

0.001892	0.000329	0.001038*	0.001791	0.00309
Db3				
7.63e-05*	8.10**e**-05	0.00029	0.000424	0.000791
Rbio1.3				
0.002809	9.33**e**-05*	0.00155	0.00042	0.001122
Rbio2.4				
5.82e-05*	8.57**e**-05	0.000224941	0.000416952	0.000696509

To facilitate imagination, we draw some data related to Table 5 in Fig. 9. According to the results, Fig. 9a shows the standard deviation produced from the wavelet coefficients at the first six scales through four wavelet functions in the Gaus wavelet family. In all scales, as vanishing moments increase, the standard deviations generated from the wavelet coefficients decrease. This statement is valid for other wavelet functions in Figs. 9c and 9d. However, in Fig. 9b, wavelet functions have only one vanishing moment. Among them, the optimal wavelet function is Morl at scale two because it produced the lowest standard deviations from the wavelet coefficients (See Table 5). Also, the worst wavelet function is Mexh, especially when the scale increases. Globally, the best wavelet function among all wavelet functions considered for scenario 2 is db1 according to Table 5.

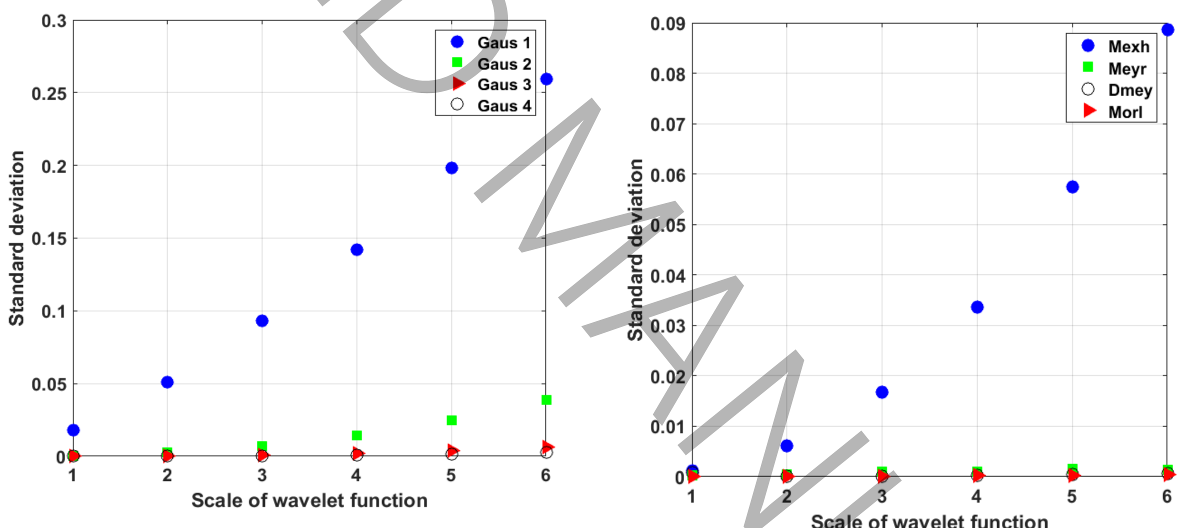

A b

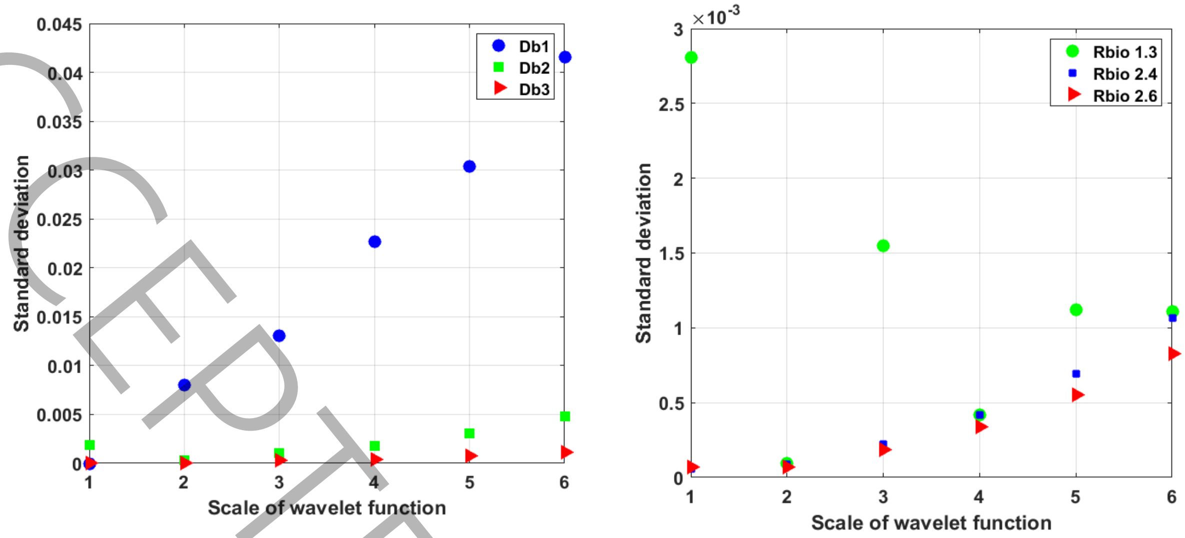

C d

Fig. 9: Standard deviation obtained from different families of wavelet functions at different scales for scenario 2

Using the same procedure, we obtain the best or optimal wavelet functions for all considered damage scenarios and list them in Table 6. As shown in Table 6, six optimal wavelet functions with their scales and the generated standard deviations are selected for the six scenarios.

Table 6: Optimal wavelet functions for the six considered scenarios

Damage Scenario	Selected Optimal Wavelet Function	Scale	Standard Deviation
1	Morl	2	3.28e-05
2	Dmey	2	5.13e-05
3	Mexh	1	0.001087
4	Db2	2	3.5476e-04
5	Coif3	2	3.10445e-05
6	Mexh	1	0.001089

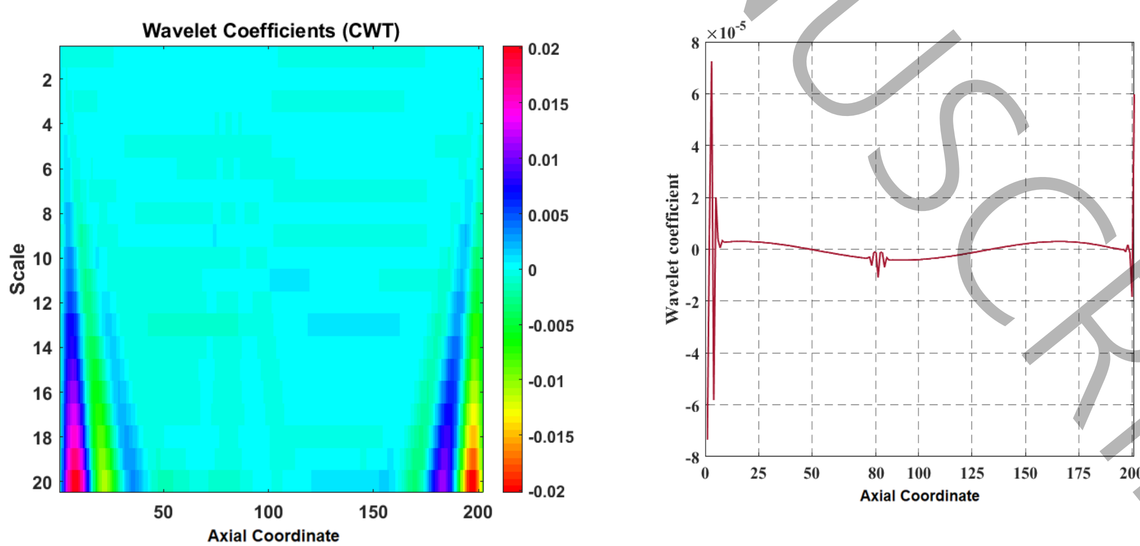

Scenario 1(CWT) Scenario 1 (Proposed Method)

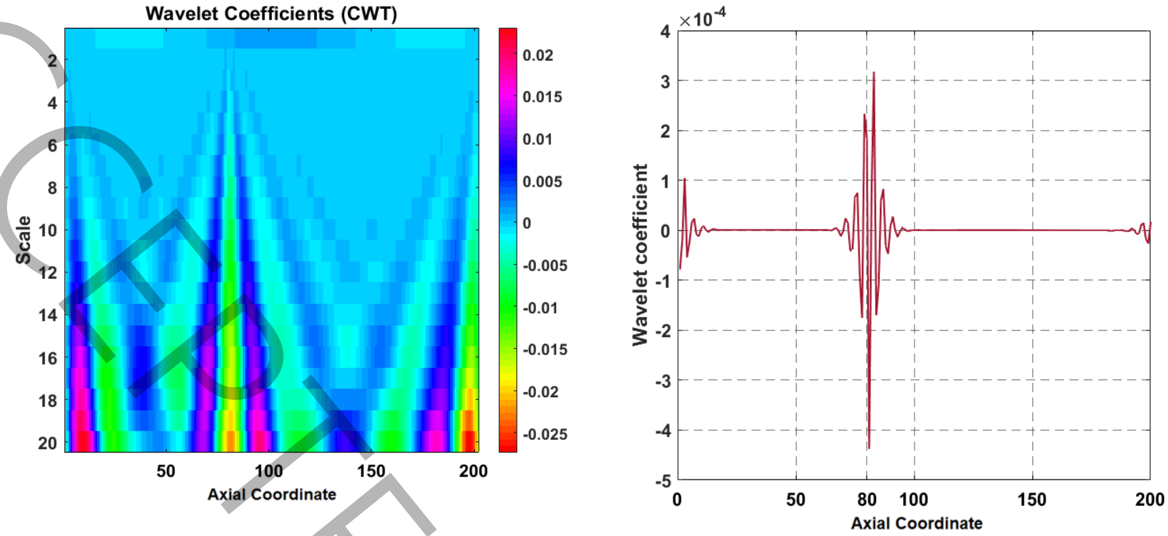

Scenario 2(CWT) Scenario 2 (Proposed Method)

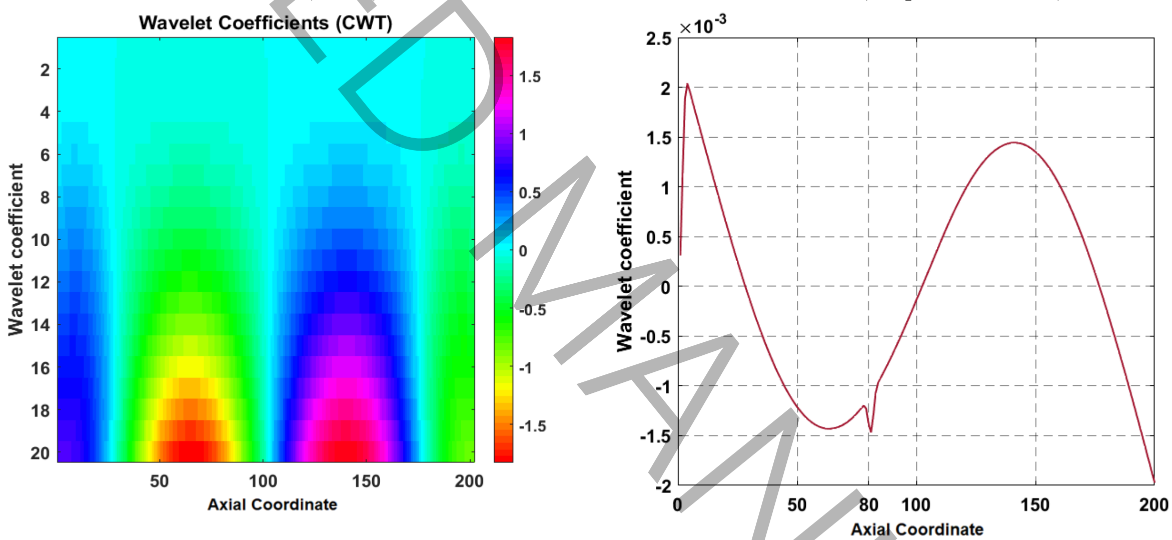

Scenario 3 (CWT) Scenario 3 (Proposed Method)

Fig. 10: Damage detection on laminated composite beam using CWT and the proposed method (S1 to S3)

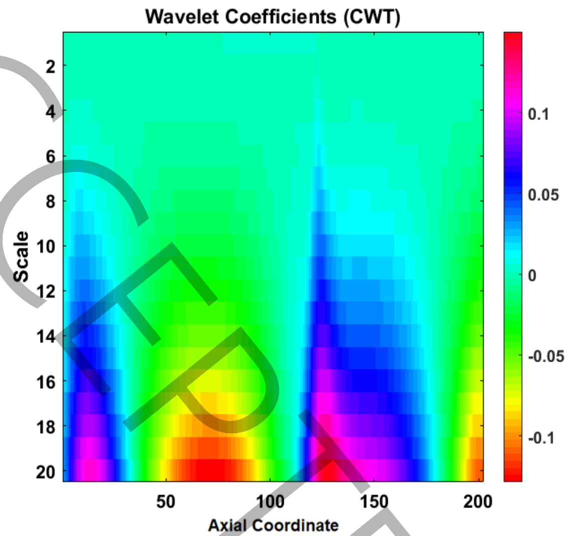

Scenario 4 (CWT)

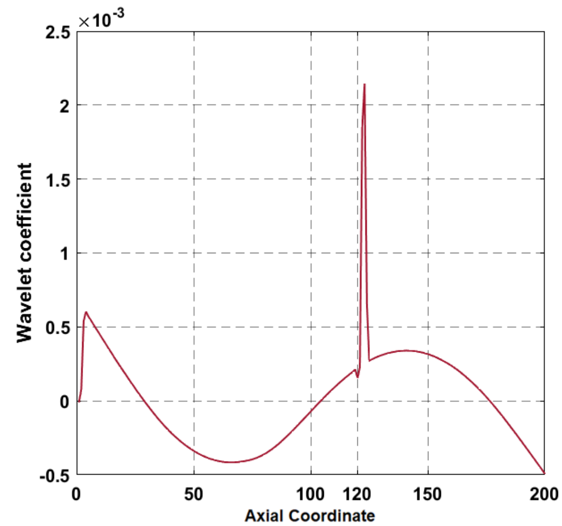

Scenario 4 (Proposed Method)

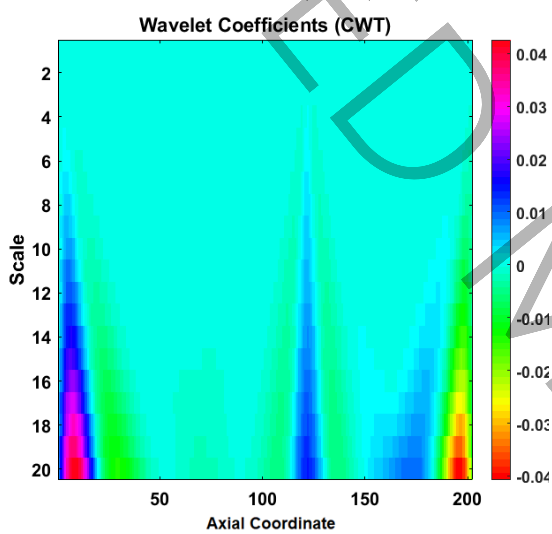

Scenario 5 (CWT)

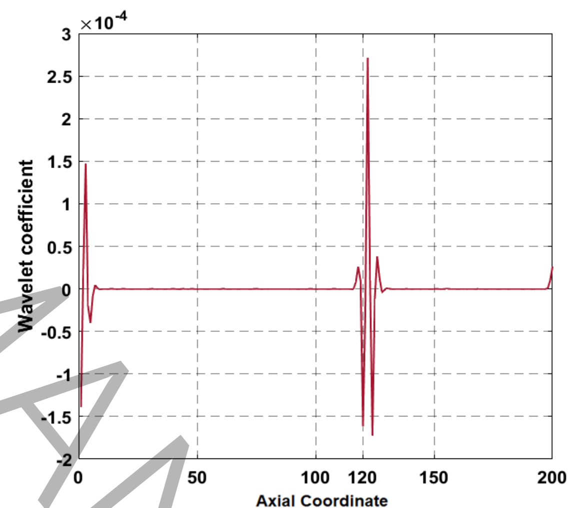

Scenario 5 (Proposed Method)

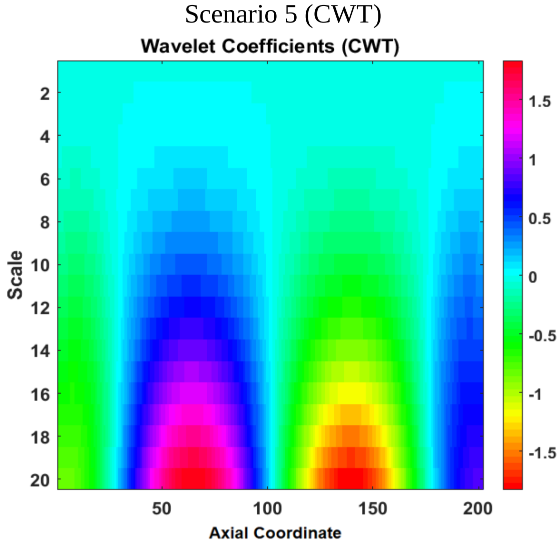

Scenario 6 (CWT)

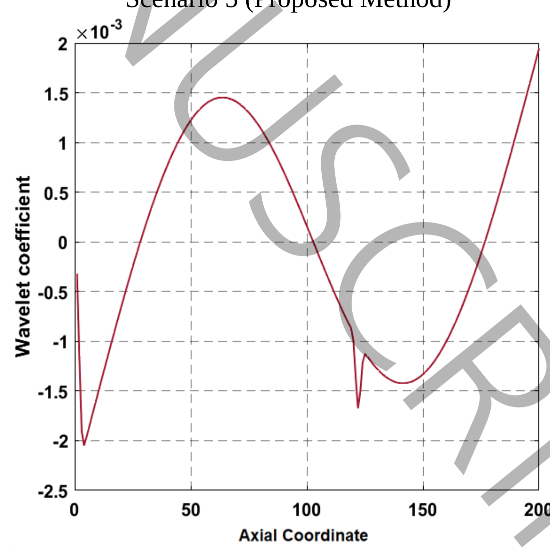

Scenario 6 (Proposed Method)

Fig. 11: Damage detection on laminated composite beam using CWT and the proposed method (S4 to S6)

Fig. 10 represents the results using CWT and the proposed method for damage scenarios 1 to 3 (i.e. S1 to S3). Also, Fig. 11 indicates the results of CWT and the proposed method for damage scenarios 4 to 6 (i.e. S4 to S6). As shown, different wavelet functions lead to different results. According to Figs. 10 and 11, the proposed methodology relying on the optimized wavelet functions can detect damages with different locations and levels with high accuracy, whereas the continuous wavelet transform (CWT) only detects the scenarios 2, 4, and 5 with low accuracy and it cannot localize damages for the scenarios 1, 3, and 6, because it suffers from redundancy in scales. Fig. 11 is the best example of the effectiveness of the proposed methodology. Fig. 11 (e.g. Scenario 6) shows that although the damage due to the redundancy of scales cannot be identified by the continuous one-dimensional wavelet (CWT) transform, our proposed method extracted the crack data based on the minimum standard deviation of the coefficients obtained from the CWT. Additionally, the damage detection results show that the range of damage detection wavelet coefficients increases as the damage level increases.

In order to validate the efficiency of the proposed method in practical applications, the next Section deals with the experimental evaluation.

4.3.2. Experimental Evaluation

A laminated composite curved beam is constructed to validate the practical performance of the proposed standard deviation-based wavelet transform damage detection method. Our laminated composite curved beam is constructed using the vacuum infusion process. In this process, a mixture of the epoxy resin and Polyepoxide-Ployamine hardener is injected into a closed mold by a vacuum pump. In the closed mold, there are eight layers of glass fibers. The use of the vacuum injection process in the composite industry is developing, and it is possible to produce high-quality laminated composite parts [39-41]. After constructing the laminated composite curved beam, it is meshed by 29 finite elements and U-shape single damage created at the twentieth element from the top of the beam, and the damage is located at the element numbers 10 and 11, as seen in Fig. 12.

After constructing, meshing the laminated composite curved beam, it is tested using the non-contact laser Doppler to obtain first experimental mode shape of it. The modal test is performed at each point of the beam separately (the vibrator is fixed at the middle point of line 23 and the laser is moved at other specified points). A random signal is used in the frequency range of 5 to 400 Hz to stimulate the dynamic behavior of the composite curved beam.

a b

Fig. 12: a) Meshing the constructed laminated composite curved beam and creating U-shape damage to it. b) Numbering the created meshes on the beam

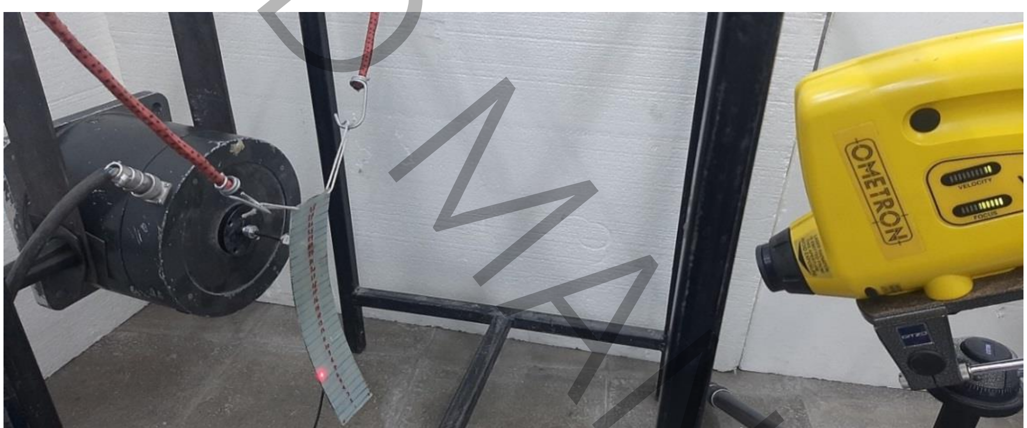

Fig. 13: Experimental modal analysis on the damaged laminated curved beam

The above test is performed at all points using a BK3560D analyzer and Pulse 8 software (Table 7).

Table 7: Characteristics of experimental modal test on the composite curved beam

Instrument name	Model
Laser Doppler Vibrometer	VH300
Shaker	BK 4808
Data acquisition equipment	BK 8200
Data acquisition software	Puls 8
FRF analyzer software	IC ATS
Sampling points	29

Type of excitation frequency	Random signal
Range of excitation frequency	5-400 Hz

Fig. 12 shows the experimental results of the proposed damage detection technique by the proposed technique.

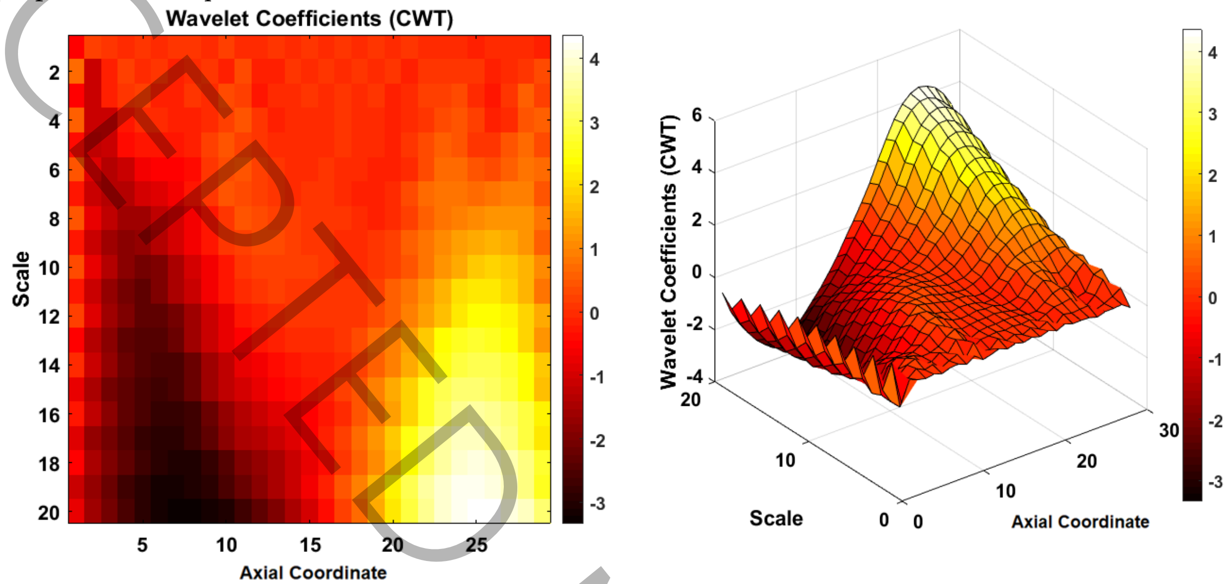

a

b

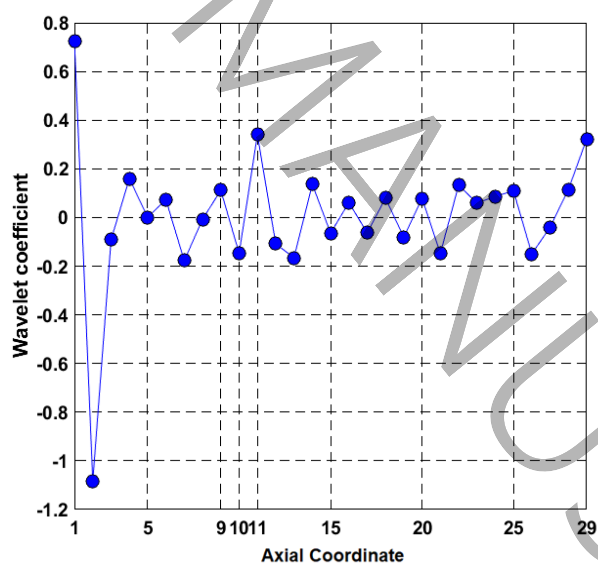

c

Fig. 14: Results of experimental damage detection scenario. a) result of CWT in two-dimensional view, b) result of CWT in three-dimensional view, and c) result of our proposed method

Figs. 14a and 14b show the results related to the experimental damage scenarios using CWT in two and three-dimensional views, respectively. As seen, the CWT cannot detect damage on the constructed laminated composite damaged curved beam. Whereas according to Fig. 14c, our proposed method can detect the location of damage with high accuracy at the sampling points 10 and 11. The wavelet function used in this scenario is db2 with the optimized scale 2. This result proves that the proposed technique is effective for experimental damage detection of the composite curved beams.

5. Conclusions

One-dimensional continuous wavelet transforms suffer from scale redundancy, which is a known weakness for fault and structural damage detection. However, the wavelet coefficients produced offer valuable information for determining the optimal wavelet scale. This paper proposes filtering these coefficients for each scale. The main findings of the current paper are listed as follows:

- Findings show that the best wavelet coefficients at a specific scale led to the minimum standard deviation. Thus, the standard deviation of the wavelet coefficients for different scales is extracted and minimized.
- Results indicate that the best scales for structural damage detection are those with lower values since the damages as the local abrupt changes in signals create high-frequency components in the signals, and the scales have an inverse relation with the frequency in signals.
- According to findings, as the vanishing moments increase, the range of the standard deviation of wavelet coefficients at a given scale decrease. This finding proves that the wavelet functions having higher vanishing moments are more suitable for structural damage detection.
- Results of this study show that the standard deviation is a sensitive index to local abrupt changes resulting from damage in the mode shape signal.
- The numerical and experimental results demonstrate the efficiency of the proposed structural damage localization in the considered curved beam that relies on the 1D-CWT.

A limitation of the current paper is that the wavelet transforms struggle to reliably detect damage in signals because their incomplete convolution at signal edges causes edge effects. Damage near these edges is therefore difficult to distinguish from these artifacts. Also, future studies should evaluate the effectiveness of the proposed wavelet selection criterion (standard deviation of wavelet coefficients) for structural damage detection using two-dimensional continuous and discrete wavelet transforms (2D-CWT and 2D-DWT). Moreover, this study can be further developed to identify damage in the vicinity of structural boundaries.

References

[1] R.A. Jafari-Talookolaei, M. Attar, P.S. Valvo, F. Lotfinejad-Jalali, S.F.G. Shirsavar, M. Saadatmorad, Flapwise and chordwise free vibration analysis of a rotating laminated composite beam, Composite Structures, 292 (2022) 115694.
[2] Ş.D. Akbaş, S. Dastjerdi, B. Akgöz, Ö. Civalek, Dynamic analysis of functionally graded porous microbeams under moving load, Transport in Porous Media, 142(1) (2022) 209-227.
[3] A. Talezadehlari, A. Nikbakht, M. Sadighi, H. Yademellat, Effect of viscoelastic interfaces on thermo-mechanical behavior of a layered functionally graded spherical vessel, AUT Journal of Mechanical Engineering, 1(1) (2017) 75-88.

[4] A. Ahmadi, M. Abedi, Transient response of laminated composite curved beams with general boundary conditions under moving force, AUT Journal of Mechanical Engineering, 6(2) (2022) 235-248.
[5] K. Khorshidi, S. Savvafi, S. Zobeid, Buckling analysis of the composite sandwich cylindrical shell integrated with auxetic metamaterial core, AUT Journal of Mechanical Engineering, 8(1) (2024) 31-42.
[6] S.A.M. Ghannadpour, M. Shakeri, A new method to investigate the progressive damage of imperfect composite plates under in-plane compressive load, AUT Journal of Mechanical Engineering, 1(2) (2017) 159-168.
[7] A. Heshmati, R.A. Jafari-Talookolaei, P.S. Valvo, M. Saadatmorad, Free and forced vibration analysis of laminated composite beams with through-the-width delamination by considering the in-plane and out-of-plane deformations, Mechanics of Advanced Materials and Structures, 31(23) (2024) 5953-5972.
[8] M. Saadatmorad, R.A. Jafari-Talookolaei, M.H. Pashaei, S. Khatir, Damage detection on rectangular laminated composite plates using wavelet based convolutional neural network technique, Composite Structures, 278 (2021) 114656.
[9] J.C.P. Allen, C.T. Ng, Damage detection in composite laminates using nonlinear guided wave mixing, Composite Structures, 311 (2023) 116805.
[10] V. Kahya, S. Şimşek, V. Toğan, Vibration-based damage detection in anisotropic laminated composite beams by a shear-deformable finite element and harmony search optimization, Structural and Multidisciplinary Optimization, 65(6) (2022) 181.
[11] A. Katunin, K. Dragan, M. Dziendzikowski, Damage identification in aircraft composite structures: A case study using various non-destructive testing techniques, Composite Structures, 127 (2015) 1-9.
[12] H. Tran-Ngoc, S. Khatir, H. Ho-Khac, G. De Roeck, T. Bui-Tien, M.A. Wahab, Efficient artificial neural networks based on a hybrid metaheuristic optimization algorithm for damage detection in laminated composite structures, Composite Structures, 262 (2021) 113339.
[13] M. Mallouli, M.B. Souf, O. Bareille, M.N. Ichchou, T. Fakhfakh, M. Haddar, Damage detection on composite beam under transverse impact using the Wave Finite Element method, Applied Acoustics, 147 (2019) 23-31.
[14] V. Kahya, F.Y. Okur, S. Karaca, A.C. Altunışık, M. Aslan, Multiple damage detection in laminated composite beams using automated model update, Structures, 34 (2021) 1665-1683.
[15] E. Manoach, S. Samborski, A. Mitura, J. Warminski, Vibration based damage detection in composite beams under temperature variations using Poincaré maps, International Journal of Mechanical Sciences, 62(1) (2012) 120-132.
[16] S. Khatir, B. Brahim, R. Capozucca, M.A. Wahab, Damage detection in CFRP composite beams based on vibration analysis using proper orthogonal decomposition method with radial basis functions and cuckoo search algorithm, Composite Structures, 187 (2018) 344-353.
[17] G. Loi, M.C. Porcu, F. Aymerich, Impact damage detection in composite beams by analysis of non-linearity under pulse excitation, Journal of Composites Science, 5(2) (2021) 39.
[18] M. Cao, P. Qiao, Damage detection of laminated composite beams with progressive wavelet transforms, Proceedings of SPIE, 6934 (2008) 693402.
[19] T. Vo-Duy, N. Nguyen-Minh, H. Dang-Trung, A. Tran-Viet, T. Nguyen-Thoi, Damage assessment of laminated composite beam structures using damage locating vector (DLV) method, Frontiers of Structural and Civil Engineering, 9(4) (2015) 457-465.

[20] W. Lestari, P. Qiao, Application of wave propagation analysis for damage identification in composite laminated beams, Journal of Composite Materials, 39(22) (2005) 1967-1984.
[21] K. Torabi, M. Shariati-Nia, M. Heidari-Rarani, Moving support technique for delamination detection in laminated composite beams using the first natural frequency, Journal of Reinforced Plastics and Composites, 36(15) (2017) 1116-1128.
[22] W. Fan, P. Qiao, A 2-D continuous wavelet transform of mode shape data for damage detection of plate structures, International Journal of Solids and Structures, 46(25-26) (2009) 4379-4395.
[23] M. Cao, P. Qiao, Integrated wavelet transform and its application to vibration mode shapes for the damage detection of beam-type structures, Smart Materials and Structures, 17(5) (2008) 055014.
[24] X. Jiang, Z.J. Ma, W.X. Ren, Crack detection from the slope of the mode shape using complex continuous wavelet transform, Computer-Aided Civil and Infrastructure Engineering, 27(3) (2012) 187-201.
[25] U.P. Poudel, G. Fu, J. Ye, Wavelet transformation of mode shape difference function for structural damage location identification, Earthquake Engineering & Structural Dynamics, 36(8) (2007) 1089-1107.
[26] S.A. Tajalli, S.M. Tajalli, Wavelet based damage identification and dynamic pull-in instability analysis of electrostatically actuated coupled domain microsystems using generalized differential quadrature method, Mechanical Systems and Signal Processing, 133 (2019) 106256.
[27] A. Heshmati, M. Saadatmorad, R.A. Jafari-Talookolaei, P.S. Valvo, S. Khatir, Damage identification in thin steel beams containing a horizontal crack using the artificial neural networks, International Conference of Steel and Composite for Engineering Structures, Springer (2022) 114-126.
[28] J.L. Vila, S.H. Carneiro, J.N. Goulart, C.T. Anflor, A.B. Jorge, Wavelet-based numerical investigation on damage localisation and quantification in beams using static deflections and mode shapes, European Journal of Mechanics - A/Solids, 107 (2024) 105351.
[29] M. Vafaei, S.C. Alih, A.B.A. Rahman, A.B. Adnan, A wavelet-based technique for damage quantification via mode shape decomposition, Structure and Infrastructure Engineering, 11(7) (2015) 869-883.
[30] M. Abdulkareem, A. Ganiyu, M.Z. Abd Majid, Damage identification in plate using wavelet transform and artificial neural network, IOP Conference Series: Materials Science and Engineering, 513 (2019) 012015.
[31] M. Saadatmorad, M.H. Shahavi, A. Gholipour, Damage detection in laminated composite beams reinforced with nano-particles using covariance of vibration mode shape and wavelet transform, Journal of Vibration Engineering & Technologies, 12(3) (2024) 2865-2875.
[32] M.R. Ashory, A. Ghasemi-Ghalebahman, M.J. Kokabi, Damage detection in laminated composite plates via an optimal wavelet selection criterion, Journal of Reinforced Plastics and Composites, 35(24) (2016) 1761-1775.
[33] M. Hajianmaleki, M.S. Qatu, Static and vibration analyses of thick, generally laminated deep curved beams with different boundary conditions, Composites Part B: Engineering, 43(4) (2012) 1767-1775.
[34] R.A. Jafari-Talookolaei, M. Abedi, M. Hajianmaleki, Vibration characteristics of generally laminated composite curved beams with single through-the-width delamination, Composite Structures, 138 (2016) 172-183.

[35] M. Rucka, K. Wilde, Application of continuous wavelet transform in vibration based damage detection method for beams and plates, Journal of Sound and Vibration, 297(3-5) (2006) 536-550.
[36] S. Mallat, W.L. Hwang, Singularity detection and processing with wavelets, IEEE Transactions on Information Theory, 38(2) (1992) 617-643.
[37] T. Ye, G. Jin, X. Ye, X. Wang, A series solution for the vibrations of composite laminated deep curved beams with general boundaries, Composite Structures, 127 (2015) 450-465.
[38] H. Sarparast, A. Ebrahimi-Mamaghani, Vibrations of laminated deep curved beams under moving loads, Composite Structures, 226 (2019) 111262.
[39] M.R. Ricciardi, V. Antonucci, M. Durante, M. Giordano, L. Nele, G. Starace, A. Langella, A new cost-saving vacuum infusion process for fiber-reinforced composites: Pulsed infusion, Journal of Composite Materials, 48(11) (2014) 1365-1373.
[40] D. Yuexin, T. Zhaoyuan, Z. Yan, S. Jing, Compression responses of preform in vacuum infusion process, Chinese Journal of Aeronautics, 21(4) (2008) 370-377.
[41] T. Gajjar, D.B. Shah, S.J. Joshi, K.M. Patel, Analysis of process parameters for composites manufacturing using vacuum infusion process, Materials Today: Proceedings, 21 (2020) 1244-1249.